REPORT DOCUMENTATION PAGE

Form Approved
OMB NO. 0704-0188

1. AGENCY USE ONLY (Leave Blank)	2. REPORT DATE November 28, 2000	3. REPORT TYPE AND DATES COVERED Final

4. TITLE AND SUBTITLE
Numerical Simulation of Nonlinear Optical Fibers

5. FUNDING NUMBERS
DAAH04-96-1- 0406

6. AUTHOR(S)
Dennis Sullivan

7. PERFORMING ORGANIZATION NAME(S) AND ADDRESS(ES)
Department of Electrical Engineering
University of Idaho, Moscow, ID 83844-1023

8. PERFORMING ORGANIZATION REPORT NUMBER
FJK224

9. SPONSORING / MONITORING AGENCY NAME(S) AND ADDRESS(ES)
U. S. Army Research Office
P.O. Box 12211
Research Triangle Park, NC 27709-2211

10. SPONSORING / MONITORING AGENCY REPORT NUMBER
ARO 36313

11. SUPPLEMENTARY NOTES
The views, opinions and/or findings contained in this report are those of the author(s) and should not be construed as an official Department of the Army position, policy or decision, unless so designated by other documentation.

12 a. DISTRIBUTION / AVAILABILITY STATEMENT
Approved for public release; distribution unlimited.

12 b. DISTRIBUTION CODE

13. ABSTRACT (Maximum 200 words) This project focused on computer simulation in three major areas. The first two projects involve three-dimensional electromagnetic simulation of the Maxwell equations. The third is quantum simulation via two-dimensional simulation of the Schroedinger equation. The first project resulted in a true three-dimensional simulation of a pulse propagating in a nonlinear optical fiber. The second project resulted in a system for three-dimensional simulation of pulses propagating through conductive apertures for the purpose of THz pulse shaping. The quantum simulation resulted in two major milestones. First, a method has been developed to determine the eigenenergies and eigenfunctions of arbitrary quantum nanstructures. And second, the simulation of the interaction of two electrons in a quantum dot has been completed.

14. SUBJECT TERMS
Nonlinear optical, optical fibers, THz pulses, Quantum seminconductor

15. NUMBER OF PAGES
76

16. PRICE CODE

17. SECURITY CLASSIFICATION OR REPORT UNCLASSIFIED	18. SECURITY CLASSIFICATION ON THIS PAGE UNCLASSIFIED	19. SECURITY CLASSIFICATION OF ABSTRACT UNCLASSIFIED	20. LIMITATION OF ABSTRACT UL

NSN 7540-01-280-5500

Standard Form 298 (Rev.2-89)
Prescribed by ANSI Std. 239-18
298-102

Enclosure 1

20010116 126

DTIC QUALITY INSPECTED 3

(1) List of Manuscripts

Refereed Journals

(i) D. M. Sullivan, "Digital filtering techniques for use with the FDTD method," *Internat. J. of Numerical Modeling,* March, 1999 (Invited Paper).

(ii) D. M. Sullivan, J. Liu, M. Kuzyk, "Three dimensional optical pulse simulation using the FDTD method," *IEEE Trans. on Microwave Theory and Tech.,* Vol. MTT-48, pp 1127-1133, July, 2000.

(iii) D. M Sullivan, J. Young, "Far field time domain calculation from aperture radiators using the FDTD method," *IEEE Trans. Antennas and Prop.,* scheduled for publication, Feb. 2000.

(iv) S. Nekkanti, D. Sullivan, D. S. Citrin, "Simulation of spatiotemporal terahertz pulse shaping in 3-D using conductive apertures of finite thickness," *IEEE J. of Quantum Electronics,* submitted for review.

(v) D. Sullivan, D. S. Citrin, "Determination of the eigenfunctions of arbitrary nanostructures using time domain simulation," *J. of Computational Physics,* submitted for review.

(vi) D. Sullivan, D. S. Citrin, "Time domain simulation of multiple particles in a quantum dot," *J. Applied Physics,* submitted for review.

Conference Abstracts

(i) D. M. Sullivan, "Three dimensional simulation of nonlinear optical phenomena," 3th Internat. Conf. on Organic Nonlinear Optics, Dec. 16-20, 1996, Marco Island, Florida.

(ii) D. M. Sullivan, "Three dimensional optical fiber simulation," 1997 IEEE Internat. Symposium on Antennas and Prop., July 13-18, 1997, Montreal, Canada.

(iii) D. M. Sullivan, "Three dimensional nonlinear optical fiber simulation, "4th International Conference on Millimeter and submillimeter waves and applications, July 20-24, 1998, San Diego, California.

(iv) D. M. Sullivan, "Three dimensional optical fiber simulation," 5th Internat. Conf. on Organic Nonlinear Optics, March 12-16, 2000, Davos, Switzerland.

Enclosure 2

(v) D. M Sullivan and J. Young, "Far field time domain calculation from aperture radiators using the FDTD method," 2000 IEEE Internat. Symposium on Antennas and Prop., July 16-21, 2000, Salt Lake City, Utah.

(vi) D. M. Sullivan and M Kuzyk, "Three-dimensional optical fiber simulation using the FDTD method," 2000 IEEE Internat. Symposium on Antennas and Prop., July 16-21, 2000, Salt Lake City, Utah.

Master's Theses

(i) J. Liu, "Three dimensional optical soliton simulation," Master of Science thesis, Dept. of Electrical Engineering, Univ. of Idaho, Fall, 1999.

(ii) S. Nekanti, "Simulation of Spatiotemporal Terahertz Pulse Shaping in Three Dimensions Using Conductive Apertures of Finite Thickness," Master of Science thesis, Dept. of Electrical Engineering, Univ. of Idaho, Spring, 2000.

(2) Scientific Personnel

(i) Dennis Sullivan, Ph. D.

(ii) Sunil Nekkanti, M. S. Student

(iii) Jun Liu, M. S. Student

(3) Report of Inventions

N/A

(4) Scientific Progress and Accomplishments

After the second year of the project, the main focus shifted from nonlinear fiber optical simulation to quantum semiconductor simulation. However, the nonlinear optical simulation was still pursued, principally by Jun Liu, a graduate student, who simulated a three dimensional optical soliton. Besides the nonlinear optical simulation and the quantum semiconductor simulation, some effort was put into applying the methods that have already been developed for use in terahertz pulse shaping. This was primarily done by another graduate student, Sunil Nikkanti. This has proved to be a very promising direction for further simulation applications.

Enclosure 2

Nonlinear Optical Fiber Simulation

A paper documenting our developments in three-dimensional optical fiber simulation has appeared in the literature. A graduate student, Jun Liu, used these developments to simulate three-dimensional soliton simulation in an optical fiber. This was his master's thesis.

Quantum Semiconductor Simulation

The quantum semiconductor simulation project has been pursued with the intention of developing quantum switching mechanisms. This is being done in collaboration with the Quantum Optics Theory Group of the Physics Department of Washington State University headed by Professor David Citrin. A time domain formulation of the Schroedinger equation has been developed. The specific configuration being simulated is a quantum dot. This was chosen because both theoretical and experimental data are available for verification of the accuracy of the simulation (R. C. Ashoori, "Electrons in Artificial Atoms," *Nature*, 379, 413-419, 1996). Two major milestones have been achieved so far:

Determination of the Eigenstates of Arbitrary Structures.

The analytical description of particles in a quantum structure is available only for the simplest canonical configurations. Using a finite-difference formulation of the Shroedinger equations, a method has been developed to determine the eigenenergies and eigenfunctions of any arbitrary quantum structure. (Please see enclosed manuscript.)

Multiple particles in a quantum dot

The interaction of two electrons in a quantum dot under the influence of a magnetic field has been simulated using Schroedinger equation and the Hartree-Folk approximation. The Hartree-Folk formulation takes into account the Coulomb interaction of the two particles as well as the exchange term, which is a purely quantum mechanical effect based on the relative spins of the two particles. The Hartree-Folk formulation is computationally very intensive, and can be analytically calculated for only the simplest cases. By reformulating the Coulomb and exchange terms as convolutions, a fast two-dimensional Fourier transform algorithm available on the Cray T90 of the San Diego Supercomputer Center has made these calculations tractable. Thus far, the interaction of two particles in a quantum dot subject to variable external magnetic field has been simulated. The resulting energy levels are found to be in agreement with those available in the literature. (Please see the enclosed manuscript.)

Enclosure 2

Simulation of Terahertz Pulse Generation

The generation of very short, high frequency pulses has become of great interest to the physics community over the past few years. The physical processes that produce terahertz (THz) pulses do not produce the short, well defined pulses for applications such as time-domain spectroscopy. They require filtering. One such filtering technique is spatiotemporal shaping in which the pulse is passed through a slot in a metal screen. This is an application well suited to simulation, where different aperture configurations can be tested without the construction of expensive and time consuming experiments. A paper appeared using the finite-difference time-domain method to do a two-dimensional simulation. [J. Bromage, et al, "Spatiotemporal shaping of half-cycle terahertz pulse by diffraction through conductive apertures of finite thickness," *J. Optical Soc. Amer. B*, vol. 15, pp 1399-1405, April, 1998.] Clearly a three-dimensional simulation is needed to account for all parameters. However, the three-dimensional simulation of the far field of the pulse from an aperture is a computationally prohibitively large problem. A method was developed to calculate the far field from an aperture while simulating only the immediate area around the aperture. (This is described in a paper.) Furthermore, the symmetry of the problem is exploited to cut the computation by one fourth. Using these methods and state-of-the-art computer resources, the three-dimensional simulation of THz pulse was accomplished. A graduate student, Sunil Nekkanti, has used this method for terahertz pulse shaping. (Please see enclosed manuscript.) This was the subject of his master's thesis.

(5) Technology Transfer

N/A

Time Domain Simulation
of Two Electrons in
a Quantum Dot

Dennis Sullivan, Ph. D.
Department of Electrical and
Computer Engineering
University of Idaho
Moscow, Idaho 83844-1023
(208) 885-5926
dennis@ee.uidaho.edu

D. S. Citrin, Ph.D.
Department of Physics
and Materials Research Center
Washington State University
Pullman, WA 99164-2814
(509) 335-3698
citrin@wsu.edu

Abstract

A time-domain simulation method is presented that utilizes the Hartree-Fock formulation to characterize two particles in a quantum dot. The basis of the simulation is the finite-difference time-domain (FDTD) method. The computation is made tractable by formulating the Coulomb and exchange terms as digital filtering problems, and utilizing two-dimensional fast Fourier transforms. Two-electron wavepacket dynamics are calculated.

I. Introduction

Semiconductor quantum dots (QD) have attracted great attention due to the quantization of carriers in three dimensions, leading to discrete spectra [1]. Among other things, they present the possibility of studying the detailed interaction of particles in a controlled environment [2]. The advent of measurement techniques, such as single-electron capacitance spectroscopy (SECS), has made possible the determination of the energy of individual particles as they are added to a QD under various conditions [3, 4].

Along with the growing body of experimental work, there have been efforts to characterize these interactions through approximation techniques [5, 6, 7]. The Hartree-Fock approximation is a particularly convenient approach for the interaction of multiple particles [6]. This paper presents a formulation of the Hartree-Fock approximation using the finite-difference time-domain (FDTD) method. The FDTD method is one of the most widely used methods in electromagnetic simulation [8, 9] and it has recently been applied to the simulation of the Schroedinger equation [9, 10]. In this paper, the simulation of two electrons is presented. This technique allows for the simulation of two-electron wavepacket dynamics as well as for the determination of energy eigenstates. The computational requirements of the Coulomb and exchange terms are partly circumvented by using signal-processing techniques and a two-dimensional fast Fourier Transform (FFT). While the resulting simulation is computationally intense, it is well within the realm of state-of-the-art computing platforms.

Section II describes the FDTD formulation of a particle in a two-dimensional harmonic oscillator in a magnetic field. This is the usual characterization of a quantum dot [2]. Section III shows results of the simulation of the first few eigenstates under the influence of a magnetic field and verifies their accuracy by comparison with analytic results. In Section IV, the implementation of the Hartree-Fock approximation for the simulation of two particles is described [11]. In Section V, the simulation of two electrons in a quantum dot is presented. The chemical potential of the first two electrons is found to be in excellent agreement with results available in the literature [1, 2].

II. FDTD Formulation of the Schroedinger Equation

Basic Formulation

We treat a QD in which the confinement in the z direction is much stronger than in the x and y directions. Thus, the energy-level separation associated with the z direction quantization is much larger than any other energy scale in the problem. We therefore assume a single z-quantized state. In addition, in the present study we neglect the spin-orbit interaction which is relatively small. (This will be topic of a future study.) The time-domain formulation of the Schroedinger equation

for a particle in a two-dimensional harmonic oscillator subject to a magnetic field in the perpendicular direction is then [12]

$$i\hbar \frac{\partial \psi(x,y)}{\partial t} = \frac{1}{2m}\left(\frac{\hbar}{i}\nabla - q \cdot A\right)^2 \psi(x,y) + V_{H.O.}(x,y) \cdot \psi(x,y), \qquad (1)$$

where $V_{H.O.}(x,y)$ is the two-dimensional harmonic oscillator potential. Equation (1) can be written

$$\frac{\partial \psi(x,y)}{\partial t} = \frac{\hbar^2}{2m\hbar}\left(\frac{d^2}{dx^2} + \frac{d^2}{dx^2}\right)i\psi(rx,y)$$

$$-\frac{B_0^2 q^2 (x^2 + y^2)}{2m\hbar}i\psi(x,y) + 2\frac{B_0 q}{2m}\left(-y\frac{d}{dx} + x\frac{d}{dy}\right)\psi(x,y) \qquad (2)$$

$$-i\frac{1}{2}\frac{E_0^2}{\hbar}(x^2 + y^2)^{1/2} \cdot \psi(x,y),$$

where E_0 is the ground state energy of the harmonic oscillator and B is the strength of the magnetic field, which is assumed to be uniform and in the z direction. Next, ψ is separated into real and imaginary parts:

$$\psi(r,t) = \psi_{real}(r,t) + i\psi_{imag}(r,t).$$

Then the finite-difference approximations to the spatial and temporal derivatives are taken. Equation (2) becomes two coupled equations, the real part given by

$$\psi^n{}_{real}(i,j) = \psi^{n-1}{}_{real}(i,j)$$

$$-\frac{\hbar}{2m}\frac{\Delta t}{\Delta x^2}\left[\begin{array}{c}-4\psi^{n-1/2}{}_{imag}(i,j) + \psi^{n-1/2}{}_{imag}(i+1,j) + \psi^{n-1/2}{}_{imag}(i-1,j) \\ + \psi^{n-1/2}{}_{imag}(i,j+1) + \psi^{n-1/2}{}_{imag}(i,j-1)\end{array}\right]$$

$$+\frac{B_0^2 q^2}{2m\hbar}\Delta t\left[\Delta x^2(i-ic)^2 + \Delta x^2(j-jc)^2\right]\psi^{n-1/2}{}_{imag}(i,j) \qquad (3)$$

$$+\frac{B_0 q}{m}\Delta t\left[\begin{array}{c}\Delta x(i-ic)\dfrac{\left(\psi^{n-1}{}_{real}(i,j+1) - \psi^{n-1}{}_{real}(i,j-1)\right)}{2\Delta x} \\ -\Delta x(j-jc)\dfrac{\left(\psi^{n-1}{}_{real}(i+1,j) - \psi^{n-1}{}_{real}(i-1,j)\right)}{2\Delta x}\end{array}\right]$$

$$+\frac{1}{2}k_0 \cdot \left[(i-ic)\cdot \Delta x + (j-jc)\cdot \Delta x\right]^2 \psi^{n-1/2}{}_{imag}(i,j).$$

There is a corresponding equation to calculate the imaginary part. Here we discretize both time and space; the time step is indexed by n, the space grid by i and j. Details of the above derivation are given in [10].

3

III. Simulation of One Particle in a Quantum Dot

In this section, we will use the techniques described in the previous section to simulate the lowest order eigenstates in a quantum dot. Following the work of Ashoori et al. [4], we will assume the dot is adequately described by a two-dimensional harmonic oscillator with a fundamental energy splitting between successive single-particle levels of 5.4 meV. The eigenstates are well known [12]. A few of the lower order states are shown in Fig. 1. For simplicity, we only plot the real part of the wavefunction ψ. We describe the states by the quantum numbers (n, l), where n, the principal quantum number, is a positive integer corresponding to the number of nodes in the wavefunction moving outward from the center, and l is the axial quantum number such that $2|l|$ is the number of nodes moving in a circle on a constant radius around the dot [2]. The integer l can be positive or negative corresponding to a waveform that is moving counterclockwise or clockwise, respectively, around the center of the dot. The energy of the function is give by [2]

$$E_{n,l} = \hbar\omega_0(2n+|l|+1). \tag{4}$$

Figure 2 is a time-lapsed simulation of the real part of the (0,1) state. Its initial energy is 10.8 meV, as calculated by Eq. (4). After 0.128 ps, it has moved one-third of a revolution counterclockwise. After 0.255 ps, it has gone two-thirds of a revolution, and after 0.383 ps, it has returned to its original position. This is not surprising, since this is the revival time corresponding to 10.8 meV. This simulation used cell sizes of 2 nm and time steps of 0.05 fs. The total simulation space was 60 by 60 cells to simulate an area of 120 by 120 nm.

Figure 3 is a similar simulation of the (0, 1) state, but with an increasing magnetic field. Now the total energy is calculated by the formula [2]

$$E_{n,l} = l\hbar\frac{\omega_c}{2} + \hbar\sqrt{\left(\frac{\omega_c}{2}\right)^2 + \omega_0} \cdot (2n+|l|+1), \tag{5}$$

where $\omega_c = eB/m$ is the cyclotron frequency. Note that when the particle is initialized without the magnetic field, the energy of 10.8 meV is evenly divided between kinetic and potential energy. The radius is 18.9 nm. (The values of energy and radius are actually expectation values of the corresponding observables.) As the magnetic field is applied, a greater portion of the energy is potential energy, and the radius becomes smaller. These two phenomena correspond to the additional confinement caused by the magnetic field. The total energies correspond closely with the analytic energy calculated by Eq.(5).

Such a simulation was made for each of the six lowest energy levels and is plotted in Fig. 4. These are the Fock-Darwin levels [1]. Results are shown for the FDTD simulation and the analytic values calculated from Eq. (5). In general, agreement is excellent. Some

4

discrepancy occurs for the (0, 2) level at magnetic field levels above 6 T. The (0, 2) function is a relatively complex one (Fig. 1), and as it is compressed into tighter radii, the spatial resolution of 2 nm is no longer adequate to maintain accuracy. Obviously, this could be overcome by a higher resolution and a larger simulation space.

IV. The Hartree-Fock Approximation

The Hartree-Fock formulation for two particles results in the following coupled equations [12]:

$$i\hbar\frac{\partial\psi_1(r_1)}{\partial t} = \frac{1}{2m}\left(\frac{\hbar}{i}\nabla_1 - q\cdot A\right)^2\psi_1(r_1) + V_{H.o.}(r_1)\psi_1(r_1)$$

$$+ \frac{e^2}{4\pi\varepsilon_0}\int dr_2 \frac{|\psi_2(r_2)|^2}{|r_1 - r_2|}\psi_1(r_2) - \frac{e^2}{4\pi\varepsilon_0}\int dr_2 \frac{\psi_2^*(r_2)\psi_1(r_2)}{|r_1 - r_2|}\cdot\psi_2(r_1)\delta_{s_1 s_2},$$

(6 a)

$$i\hbar\frac{\partial\psi_2(r_2)}{\partial t} = \frac{1}{2m}\left(\frac{\hbar}{i}\nabla_2 - q\cdot A\right)^2\psi_2(r_2) + V_{H.o.}(r_2)\psi_2(r_2)$$

$$+ \frac{e^2}{4\pi\varepsilon_0}\int dr_1 \frac{|\psi_1(r_1)|^2}{|r_1 - r_2|}\cdot\psi_2(r) - \frac{e^2}{4\pi\varepsilon_0}\int dr_1 \frac{\psi_1^*(r_1)\psi_2(r_1)}{|r_1 - r_2|}\cdot\psi_1(r_2)\delta_{s_1 s_2}.$$

(6 b)

In each equation, the third term on the right is the Coulomb potential and the last term is the exchange term. $\delta_{s_1 s_2}$ is the Kroneker delta relating the spins s_1 and s_2 of the particles. Only when the spins are in the same direction does the exchange term enter into the calculations. Both ψ_1 and ψ_2 are complex variables, and each equation results in two separate equations, similar to those described in the previous section. However, they are coupled by the Coulomb and exchange terms. Note that each of these integrals is a spatial integral that must be calculated for each position in the problem space. This threatens to overwhelm the computation. This is largely overcome by recasting these integrals as convolutions and using a fast two-dimensional Fourier transform for the calculation.

We begin by taking the Coulomb integral of the first equation, Eq. (6a), which we will call $I_{C1}(r_1)$,

$$I_{C1}(r_1) = \int dr_2 \frac{|\psi_2(r_2)|^2}{|r_1 - r_2|} = \int dr_2\, h(r_1 - r_2)f(r_2)$$

(7)

where

$$h(r_1 - r_2) = \frac{1}{|r_1 - r_2|}$$

and

5

$$f(r_2) = |\psi_2(r_2)|^2.$$

This can be written in the xy co-ordinates as

$$I_{C1}(x_1, y_1) = \int dx_2 \int dy_2 \, h(x_1 - x_2, y_1 - y_2) f(x_2, y_2).$$

Convolution in the spatial domain gives multiplication in the k domain, so taking the two-dimensional Fourier transforms of Eq. (7) gives

$$I_{C1}(k_{x_1}, k_{y_1}) = H(k_{x_1}, k_{y_1}) \cdot F(k_{x_1}, k_{y_1}).$$

We have eliminated the integration. Of course, a two-dimensional Fourier transform must be carried out at every time step to get $F(k_{x_1}, k_{y_1})$ because the corresponding value of $f(x_2, y_2) = |\psi_2(x_2, y_2)|^2$ is updated at every time step; then an inverse transform is performed to get $I(x_1, y_1)$. ($H(k_{x_1}, k_{y_1})$ need only be calculated once at the beginning of the program.) Fast Fourier transforms are usually implemented in specialized subroutines that use complex arrays. Since the calculation of the Coulomb potential involves only real numbers, both Coulomb integrals can be calculated at once, one in the real buffer and one in the imaginary buffer.

Now we turn our attention to the calculation of the exchange terms. The two exchange terms of Eqs. (6 a) and (6 b) are

$$I_{Ex1} = \int dr_2 \, \frac{\psi_2^*(r_2)\psi_1(r_2)}{|r_1 - r_2|}, \tag{8 a}$$

$$I_{Ex2} = \int dr_1 \, \frac{\psi_1^*(r_1)\psi_2(r_1)}{|r_1 - r_2|}. \tag{8 b}$$

Note that r_2 and r_1 in Eqs. (8 a) and (8 b) are just integration parameters. If they were both set to r, for instance, then we can see that (8 a) and (8 b) are just complex conjugates of each other. Therefore, it is only necessary to calculate one integral and take the complex conjugate of it to get the other. Of course, we will use the same basic approach as used in the calculation of the Coulomb potentials: take the FFT of $\psi_2^*(r_2)\psi_1(r_2)$, multiply it by the transformed version of the function $1/|r_1 - r_2|$, and take the inverse FFT of the result.

The following is the procedure that must take place at every time step:

1) One forward FFT to get the Fourier transform of the magnitudes of $|\psi_1(r_1)|^2$ and $|\psi_2(r_2)|^2$, a multiplication by $H(k_{x_1}, k_{y_1})$, and then an inverse FFT to get the two Coulomb integrals.

2) A forward FFT of $\psi_2^*(r_2)\psi_1(r_2)$, multiplication by $H(k_{x_1}, k_{y_1})$, and an inverse FFT to get the exchange term for $\psi_1(r_1)$. The exchange term for $\psi_2(r_2)$ is just the complex conjugate.

6

V. Simulation of Two Particles in a Quantum Dot

In this section, we use the FDTD formulation of the Hartree-Fock approximation described in the previous section to simulate two electrons in a quantum dot as described by the two-dimensional harmonic oscillator potential. We also use the same configuration in the FDTD program, i. e., a cell size of 2 nm, a time step of 0.05 fs, and a total problem space that is 60 by 60 cells. The difference is that there are two simultaneous simulations that are coupled [Eqs. (6a) and (6b)]. As a reference, we start with the simulation of two electrons, initially at the (0,0) state and the (0,-1) state, without the Coulomb or exchange coupling (Fig. 5). In both cases, the energy is evenly divided between kinetic and potential. Figure 6 is the same two states, but with only the Coulomb interaction. (This corresponds to the case where the particles have opposing spins.) The (0,0) particle has not changed substantially but the (0,-1) has effectively been pushed outward, in keeping with the Coulomb repulsion. This is evidenced by the radius, which has increased, and the fact that the particle has substantially increased its potential energy since it was pushed further outward where the potential is higher. Note also that, besides the energies of the individual particles, there is a Coulomb energy due to their interaction. Figure 7 shows the same two particles with both Coulomb and exchange interactions, corresponding to the case where the particles have the same spin. Notice that the exchange interaction tends to pull the particles together as evidenced by the increase in radius of the (0,0) particle and decrease of the radius of the (0,-1) particle compared to Fig. 6. Note also that the Coulomb energy has increased with this increased closeness, but the exchange energy is a negative quantity that reduces the total energy of the system.

The recent development of the single-electron capacitance spectroscopy (SECS) technique allows experimentalists to observe the energy levels of individual electrons being added to a quantum dot [3]. This technique records the energy needed to add an electron under the influence of a magnetic field, a quantity known as the chemical potential. We will attempt to use the FDTD method to simulate the behavior of the first two electrons.

Or course, the first particle is just the lowest level of the Fock-Darwin level model in Fig. 4. It is repeated as the dashed line labeled "First Particle" in Fig. 8. For the second electron, we must account for the Coulomb interaction in all cases and the exchange interaction when the particles have the same spins. For instance, we may assume that the first particle has spin up, since this is the lowest energy state when the magnetic field is applied. Therefore, the second particle will start in the (0,0) state with spin down. It will have Coulomb but no exchange interaction with the first particle. The additional energy to the system is plotted as the dash-dot line labeled "Singlet" in Fig. 8. Remember, this is the chemical potential, so it is the energy of the second particle itself, plus the Coulomb energy. Suppose the second particle were a (0,-1) state with spin up. It would have a Coulomb and an exchange interaction with the first

7

particle. The additional energy as a function of the magnetic field is plotted as the solid line labeled "Triplet" in Fig. 8. Note that these two lines intersect at about 1.1 T, indicated by the arrow. These two lines are needed to simulate the second particle, because the particle starts in state (0,0), spin down, and after the magnetic field reaches 1.1 T, it flips its spin and goes to the lower (0,-1) state.

Palecios et al. [5] carried out a theoretical study using exact diagonalization and the unrestricted Hartree-Fock approximation for up to 15 electrons. Their data, along with that of the FDTD simulation, are plotted in Fig. 9 for the first two electrons. (The two lines of the second particle from Fig. 8 have been consolidated to one, but the arrow still marks the crossover points.) Clearly, the agreement is very good.

VI. Conclusion

We have presented explicit space- and time-domain Hartree-Fock simulations of two-electron wavepacket dynamics in quantum dots based on the FDTD method. From these simulations, we have extracted the eigenstates and eigenenergies. The results are in excellent agreement with the existing values in the literature.

Although the calculations presented here do not in and of themselves yield new physical results, the power of the FDTD technique must be borne in mind. As an explicit space-domain technique, one can avoid difficulties associated with constructing single-particle orbitals, which are used in computations based on Slater determinants [13]. Although we chose a parabolic confinement potential, there is no additional cost in choosing any other potential. A Slater-determinant-based calculation would require computing the single-particle orbitals for each potential chosen. Of course, the tradeoff is in the size of the spatial mesh chosen for our calculations.

The calculations presented here are also easily generalized to more particles; we estimate that for the values of the parameters used here, up to four electrons should not be too computationally taxing. In addition, simulations including spin-orbit coupling are under way and will be the topic of a future publication. Finally, a time-domain approach allows one to explore manifestly dynamical properties, such as wavepacket dynamics or the response to time-dependent fields.

8

REFERENCES

1. J. Jacak, P. Hawrylak, and A. Wojs, *Quantum Dots,* Springer, Berlin, 1997.

2. R. C. Ashoori, Nature, **379**. 413 (1996).

3. R. C. Ashoori, H. L. Stoermer, J. S. Weiner, L. N. Pfeifer, S. J. Pearton, K. W. Baldwin, and K. West, Phys. Rev. Lett., **68,** 613 (1992).

4. R. C. Ashoori, H. L. Stoermer, J. S. Weiner, L. N. Pfeifer, K. W. Baldwin, and K. West, Phys. Rev. Lett., **71,** 613 (1993).

5. J. J. Palacios, L Martin-Moreno, G. Chiappe, E. Louis, and C. Tejdor, Phys. Rev. B, **47,** 5760 (1994).

6. P. A. Maksym and T. Chakrabory, Phys. Rev. Lett., **65,** 108 (1990).

7. M. Wagner, U. Merkt, and A. V. Chaplik, Phys. Rev B, **45,** 1951 (1992).

8. A. Taflove, *Computational Electrodynamics--the Finite-difference Time-domain Method,* Artech House, Boston, 1995.

9. D. Sullivan, *Electromagnetic Simulation Using the FDTD Method*, IEEE Press, Piscataway, NJ, 2000.

10. D. M. Sullivan and D. S. Citrin, IEEE J. of Quantum Electronics, submitted for review.

11. N. W. Ashcroft and N. D. Mermin, *Solid State Physics,* Saunders College Publishing, Orlando, FL, 1976.

12. C. Cohen-Tannoudji, B. Diu, and F. Laloe, *Quantum Mechanics,* John Wiley and Sons, New York, 1977.

13. L. Joensson, M. M. Steiner, and J. W. Wilkins, Appl. Phys. Lett, **70,** 1140, (1997).

Figure Captions

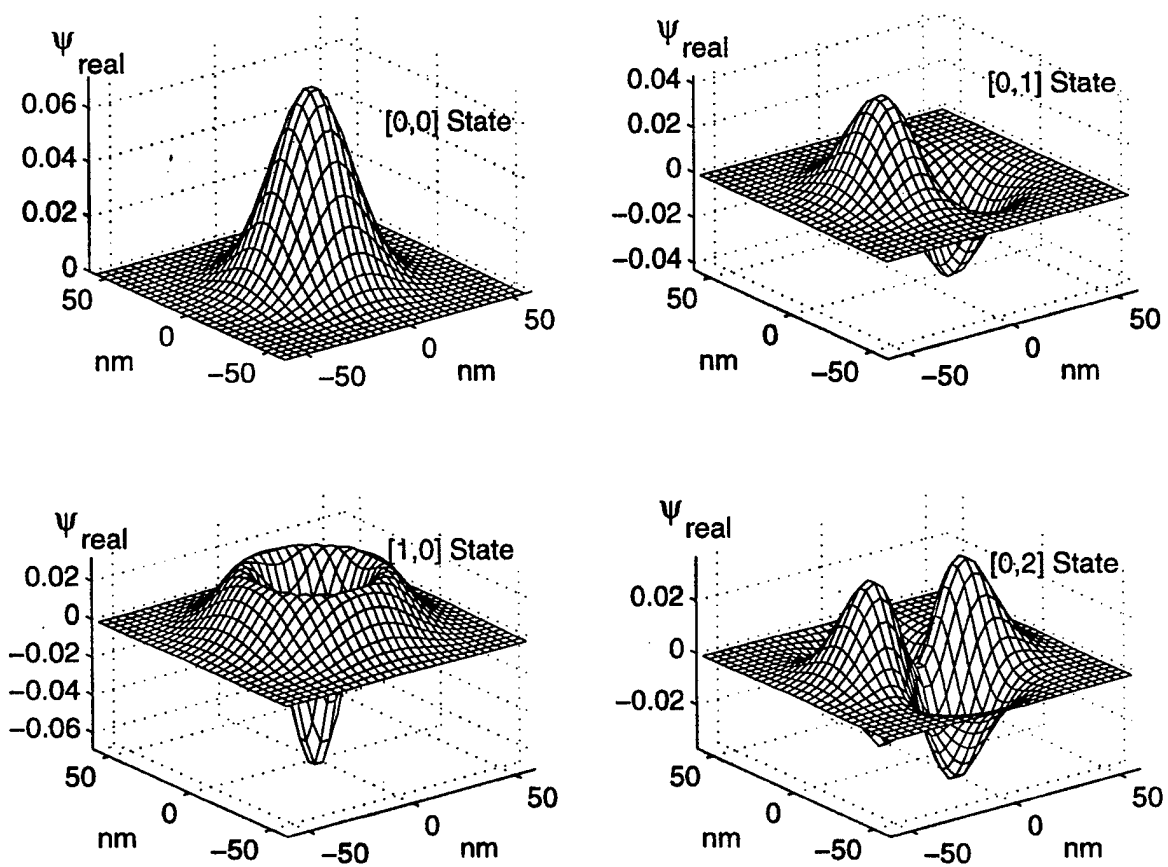Figure 1   The real part of the wave functions of four of the lowest eigenstates of a two-dimensional harmonic oscillator with a ground state of 5.4 meV.

Figure 2   The time evolution of the real part of the wavefunction of the (0,1) state through one revival. Note that the wavefunction moves counterclockwise. The imaginary part of this wavefunction is identical, but the lobes are 90 degrees out of phase to the real function shown here. The wavefunction of the (0,-1) state would move in exactly the same way, but in the clockwise directions.

Figure 3   Contour plot of the real part of the waveform for the (0,1) state with an increasing magnetic field in the perpendicular direction. The increased B field leads to a tighter confinement, as evidenced by the smaller radii and the increase in energy. (Energies are in meV, radii are in nm.)

Figure 4   Plot of the Fock-Darwin levels for a two dimensional harmonic oscillator with a ground state energy of 5.4 meV.

Figure 5   The real parts of the wavefunctions of the (0,0) and (0,-1) states of the two-dimensional harmonic oscillator. On the left side are mesh diagrams and on the right side are contour plots of the same functions. These are two independent particles, i.e., there is neither a Coulomb nor an exchange interactions.

Figure 6   The same two particles as shown in Fig. 5, but with the Coulomb interactions added (This corresponds to two particles with opposite spins). The Coulomb repulsion has added to the energy of each particle. The radius of the (0,-1) particle has increased substantially because it has been pushed outwards. In addition to the kinetic and potential energies of each particle, there is an energy of 6.67 meV associated with the repulsion of the two particles to each other.

Figure 7   The same two particles as shown in Fig. 5, but with both the Coulomb and exchange interactions added (The two particles have the same spins). The exchange has decreased the energy of each particle. The radius of the (0,-1) particle has moved a little back towards the center. In addition to the kinetic and potential energies of each particle, there is an energy of 7.38 meV associated with the repulsion of the two particles to each other and one of -2.58 meV associated with the exchange force.

Figure 8   The chemical potential as function of the magnetic field for the first two particles in a quantum dot. The plot of the first particle is simply the lowest level of the Fock-Darwin plot of Fig. 4. The second particle, however, starts off in the singlet configuration of the (0,0) state and flips its spin to the triplet configuration to take advantage of the lower energy level of the (0,-1) state as the magnetic field increases above 1.1 T.

Figure 9   Comparison of the simulated FDTD data (as shown by solid lines) and the calculated data of Palacious et al. [5] (as shown by the asterisks).

Figure 1. The real part of the wave functions of four of the lowest eigenstates of a two-dimensional harmonic oscillator with a ground state of 5.4 meV.
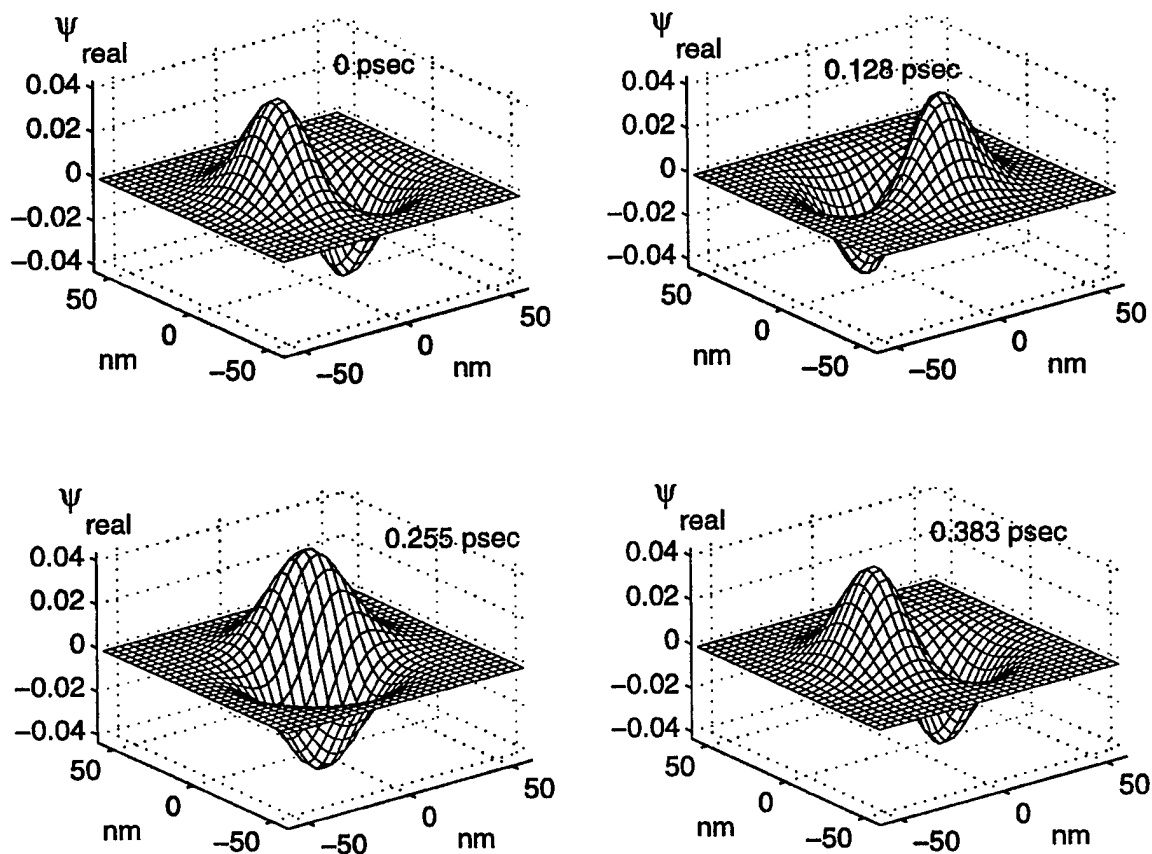
Figure 2   The time evolution of the real part of the wavefunction of the (0,1) state through one revival.   Note that the wavefunction moves counterclockwise.   The imaginary part of this wavefunction is identical, but the lobes are 90 degrees out of phase to the real function shown here.   The wavefunction of the   (0,-1) state would move in exactly the same way, but in the clockwise directions.
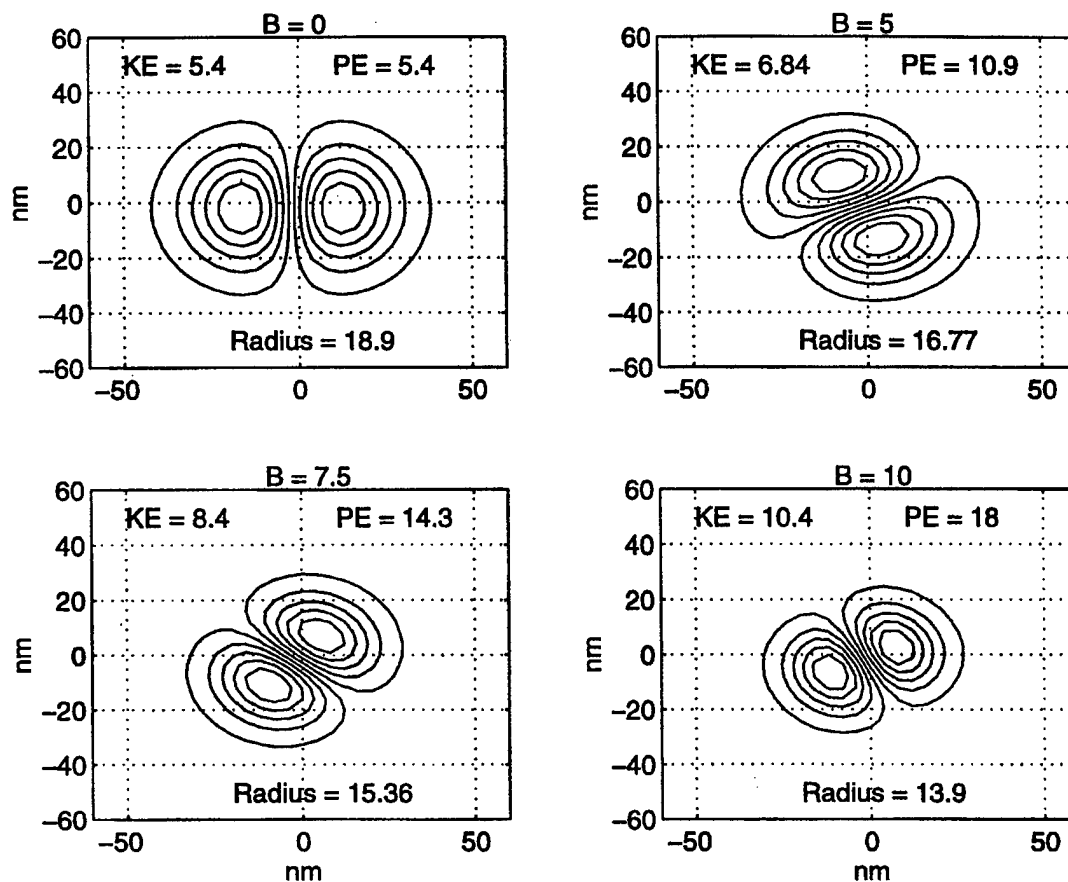
Figure 3. Contour plot of the real part of the waveform for the (0,1) state with an increasing magnetic field in the perpendicular direction. The increased B field leads to a tighter confinement, as evidenced by the smaller radii and the increase in energy. (Energies are in meV, radii are in nm.)
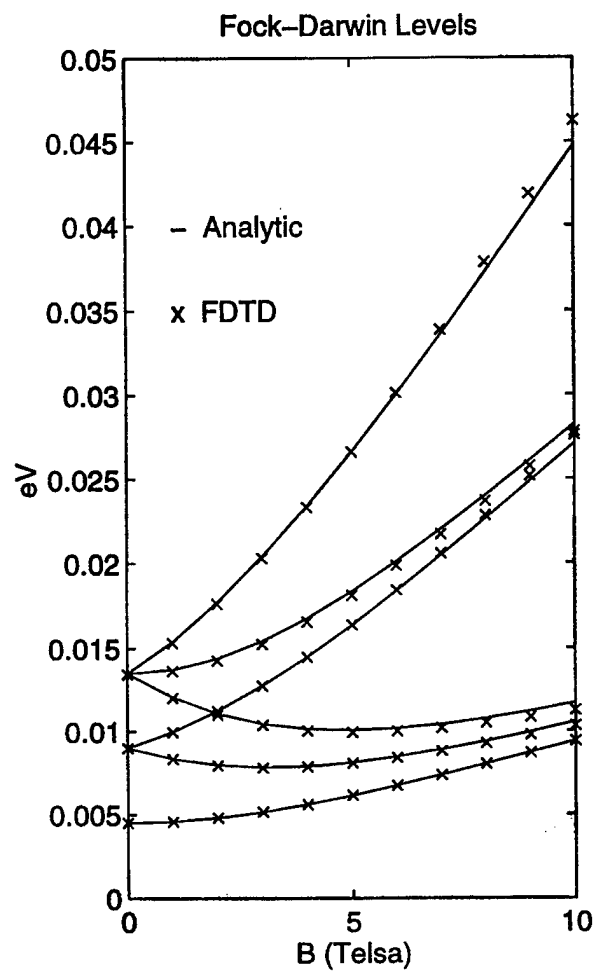
Figure 4. Plot of the Fock-Darwin levels for a two-dimensional harmonic oscillator with a ground state energy of 5.4 meV.
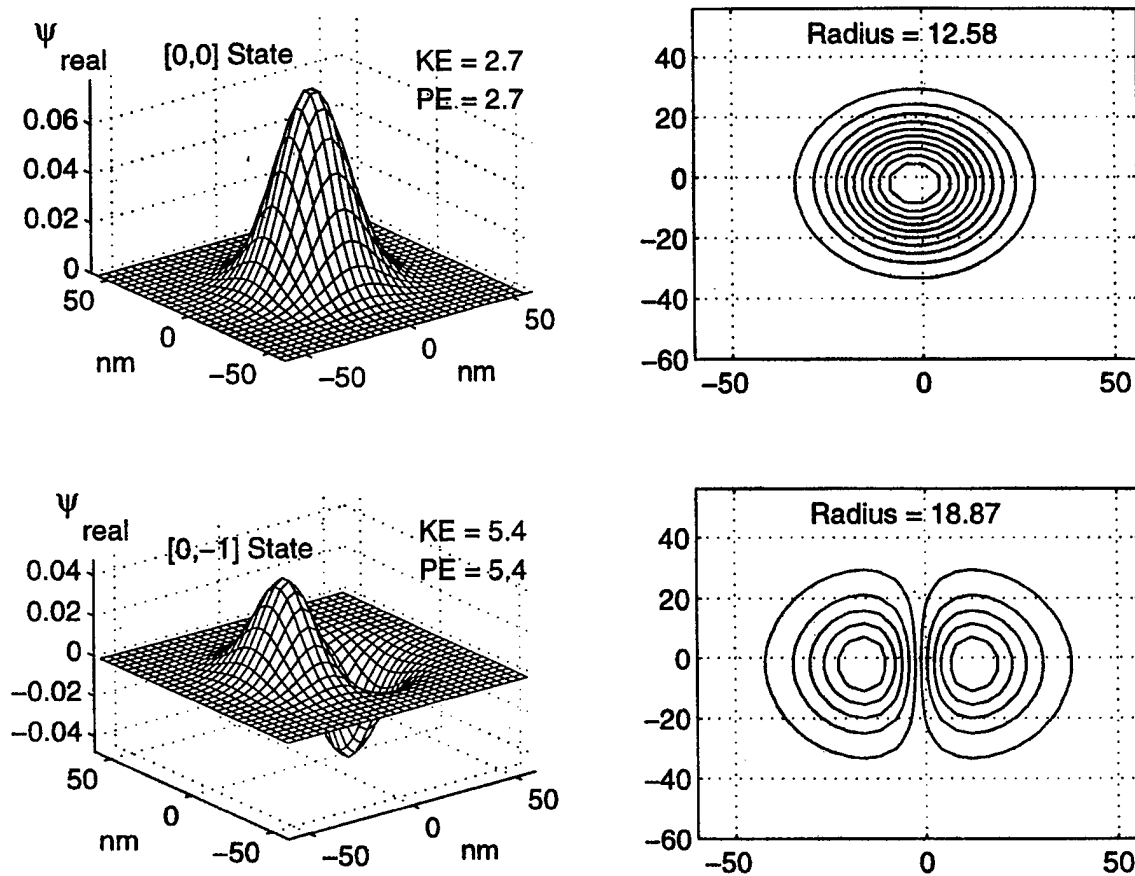
Figure 5. The real parts of the wavefunctions of the (0,0) and (0,-1) states of the two dimensional harmonic oscillator. On the left are the mesh diagrams and one the right are the contour plots of the same functions. These are two independent particles, i.e., there is neither a Coulomb nor an exchange interactions.
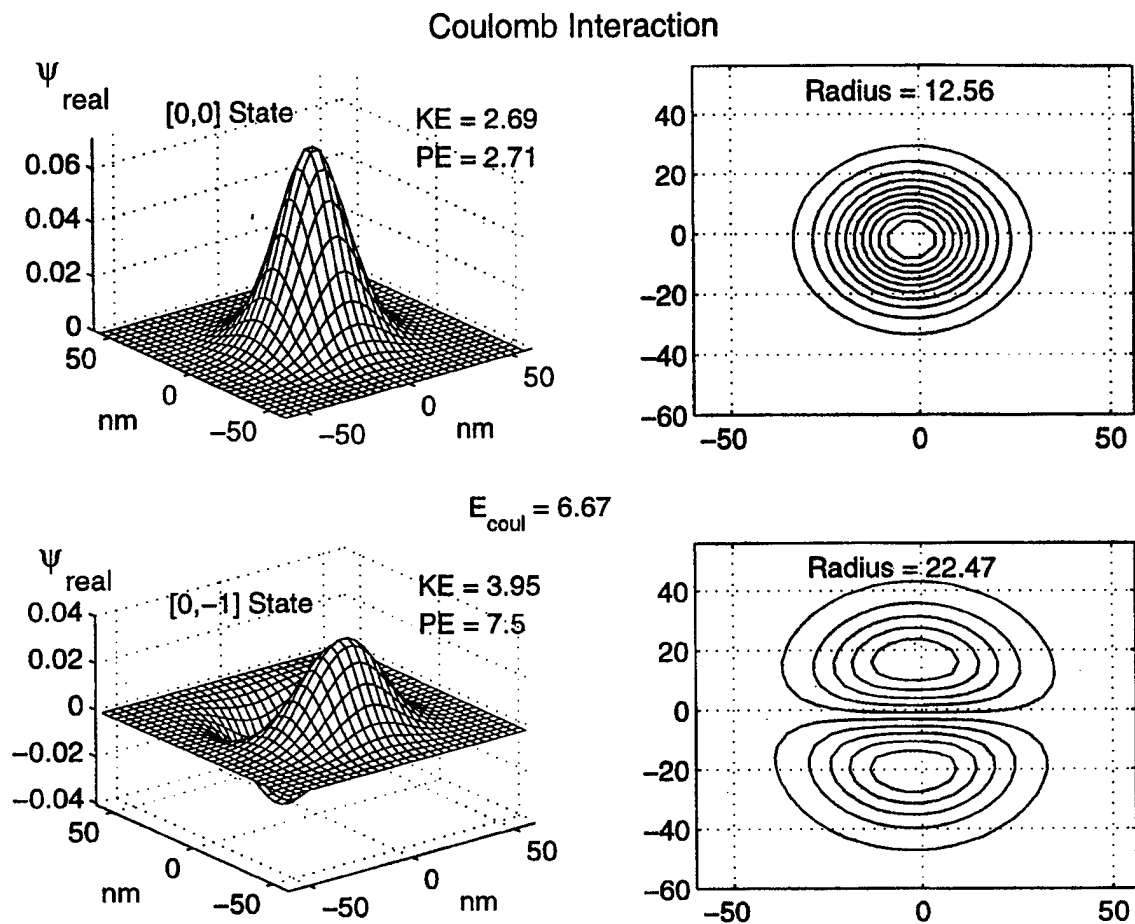
Coulomb Interaction

Figure 6. The same two particles as shown in Fig. 5, but with the Coulomb interactions added (This corresponds to two particles with opposite spins). The Coulomb repulsion has added to the energy of each particle. The radius of the (0,-1) particle has increased substantially because it has been pushed outwards. In addition to the kinetic and potential energies of each particle, there is an energy of 6.67 meV associated with the repulsion of the two particles to each other.

Coulomb and Exchange Interactions

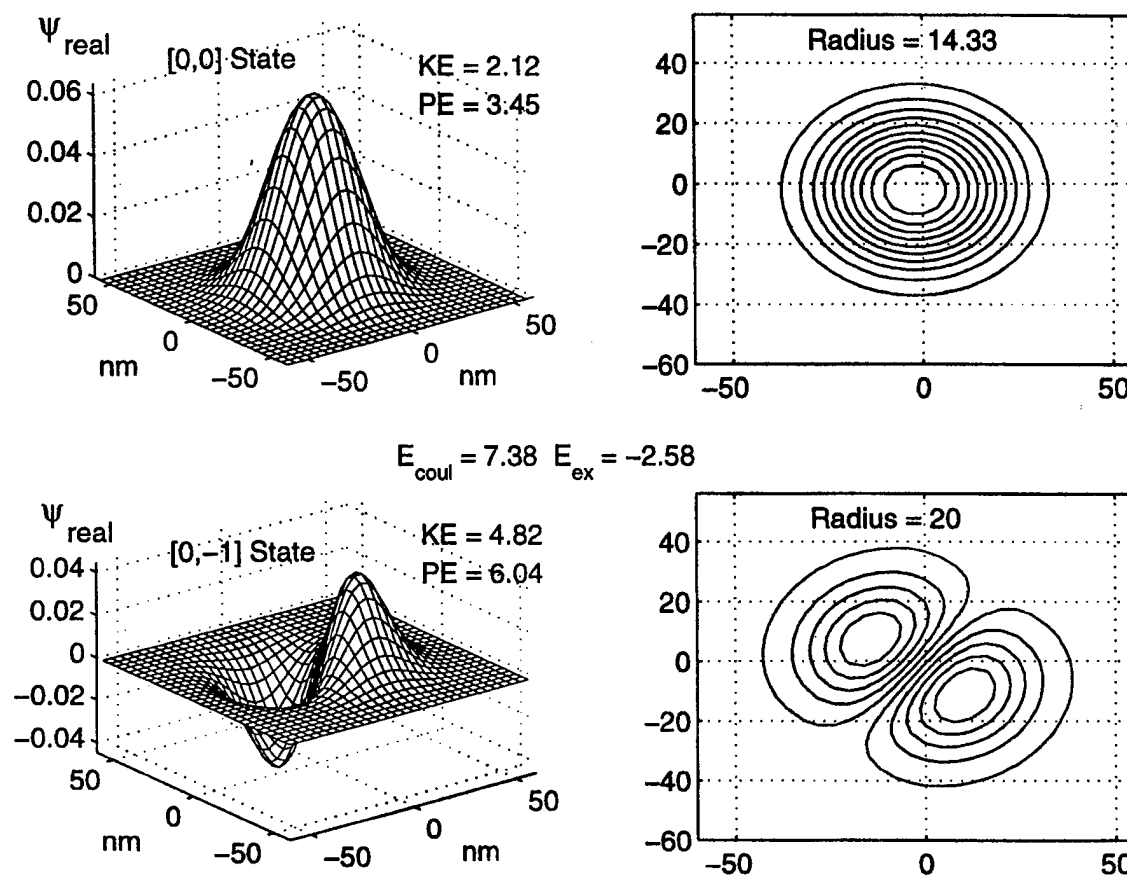$E_{coul} = 7.38 \quad E_{ex} = -2.58$

Figure 7. The same two particles as shown in Fig. 5, but with both the Coulomb and exchange interactions added (The two particles have the same spins). The exchange has decreased the energy of each particle. The radius of the (0,-1) particle has moved a little back towards the center. In addition to the kinetic and potential energies of each particle, there is an energy of 7.38 meV associated with the repulsion of the two particles to each other, and one of -2.58 meV associated with the exchange force.
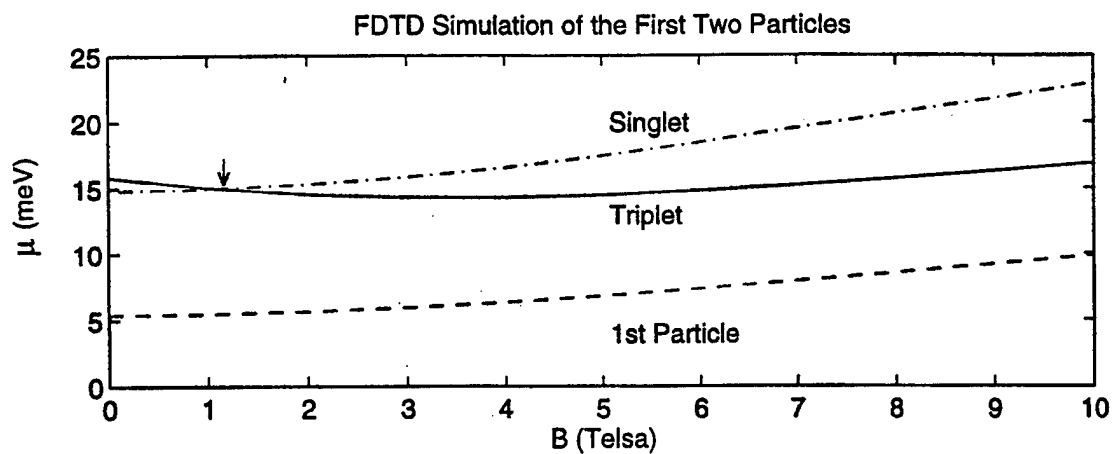
FDTD Simulation of the First Two Particles

Figure 8. The chemical potential as function of the magnetic field for the first two particles in a quantum dot. The plot of the first particle is simply the lowest level of the Fock-Darwin plot of Fig. 4. The second particle, however, starts off in the singlet configuration of the (0,0) state and flips its spin to the triplet configuration to take advantage of the lower energy level of the (0,-1) state as the magnetic field increases above 1.1 T.
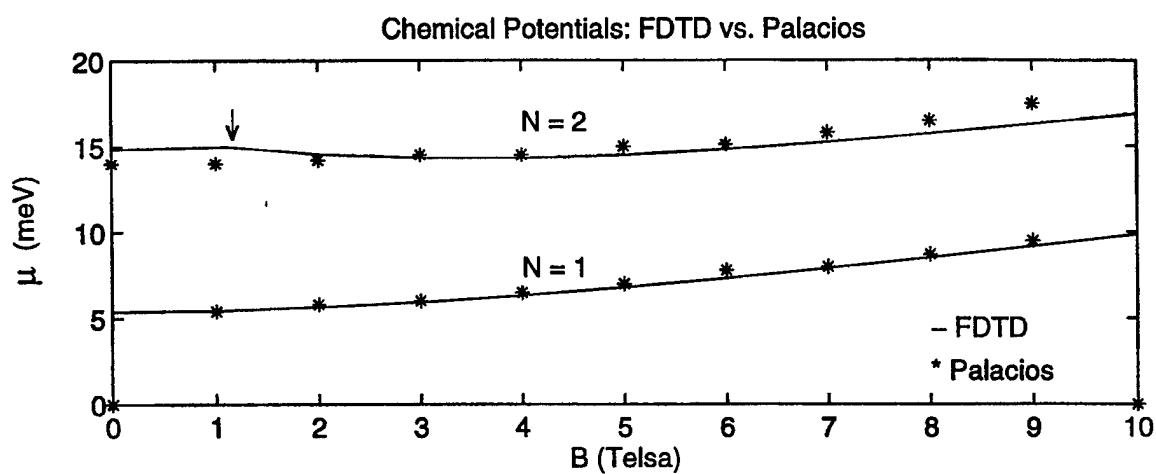
Chemical Potentials: FDTD vs. Palacios

Figure 9. Comparison of the simulated FDTD data (as shown by solid lines) and the calculated data of Palacious et al. [5] (as shown by the asterisks).

Determination of the Eigenfunctions of Arbitrary Nanostructures Using Time Domain Simulation

Dennis Sullivan, Ph. D.
Department of Electrical and
Computer Engineering
University of Idaho
Moscow, ID 83844-1023
(208) 885-5926
FAX (208) 885-7579
dennis@ee.uidaho.edu

D. S. Citrin, Ph.D.
Department of Physics
and Materials Research Center
Washington State University
Pullman, WA 99164-2814
(509) 335-3698
citrin@wsu.edu

1

Abstract

With the present interest in nanostructures, such as quantum dots, a need exists to have a flexible method to be able to determine eigenvalues and eigenstates for those structures that do not lend themselves to existing analytical methods. In this paper we present a method that accomplishes this by using a simulation of the Schroedinger equation based on the finite-difference time-domain (FDTD) method. This method is capable of simulating any structure within the limits of discritization. By initializing a simulation with a test function, the eigenfrequencies are determined through a Fourier transform of the resulting time-domain data collected at a sample point. Another simulation implements a discrete Fourier transform at the eigenfrequencies at every cell in the problem space, from which the eigenfunctions can be constructed.

I. Introduction

There is an increasing interest in semiconductor structures on the order of hundreds of nanometers as potential computing devices and for other applications [1]. However, for anything but the simplest canonical structures, a solution for the quantum mechanical states of electrons is difficult. For this reason, numerical rather than analytic approaches must be used to determine the eigenenergies and eigenfunctions of such structures.

In this paper we present a formulation using the finite-difference time-domain (FDTD) method [2, 3]. This method is widely used in electromagnetic simulation. Here we present the FDTD formulation of the Schroedinger equation; an explicit method that begins with the time-domain Schroedinger equation and approximates the temporal and spatial derivatives as difference equations [3]. In this formulation, the potential need not be a simple structure (e.g. a harmonic oscillator or square well); any arbitrary configuration can be simulated. Furthermore, the influence of a magnetic field is described. The expectation values of observables, such as kinetic and potential energy, can be easily calculated.

The determination of eigenenergies is accomplished by storing the time-domain data from a test point during a simulation and determining the eigenfrequencies by post processing, i.e., taking the Fourier transform of the stored time-domain data. The eigenfunctions are reconstructed by rerunning the simulation and taking a discrete Fourier transform at the previously determined eigenfrequencies. This is accomplished by initializing the problem space with a test function and then carrying out a discrete Fourier analysis at the eigenfrequencies at every point in the problem space [4, 5]. At the end of the simulation, one has the amplitudes and phases of the eigenfunctions at every point within the problem space for each eigenfrequency. From this information, one can determine the eigenfunctions.

We begin with a description of the FDTD formulation of the Schroedinger equation. As an initial example, we describe the simulation of a quantum dot, which is implemented by a two-dimensional harmonic oscillator simulation [6]: the third dimension can be assumed to be well confined. From the standpoint of the numerical technique, there is nothing special about a harmonic oscillator potential. We use this to illustrate the method because it has an analytic solution, from which we can verify the accuracy of the FDTD simulation.

Finally, we take a "stadium" potential to use the full power of the method to determine the low lying eigenfunctions in a structure for which there is no analytic solution.

II. FDTD Formulation of the Schroedinger Equation

Basic Formulation

The time dependent Schroedinger equation is given by [7]

$$i\hbar \frac{\partial \psi(r,t)}{\partial t} = -\frac{\hbar^2}{2m} \nabla^2 \psi(r,t) + V(r,t) \cdot \psi(r,t)$$

or

$$\frac{\partial \psi(r,t)}{\partial t} = i\frac{\hbar}{2m} \nabla^2 \psi(r,t) - \frac{i}{\hbar} V(r,t) \cdot \psi(r,t). \tag{1}$$

To avoid using complex numbers, we will split the variable $\psi(r,t)$ into its real and imaginary components:

$$\psi(r,t) = \psi_{real}(r,t) + i\psi_{imag}(r,t). \tag{2}$$

Inserting Eq. (2) into Eq. (1) and separating the real and imaginary parts results in the following coupled set of equations:

$$\frac{\partial \psi_{real}(r,t)}{\partial t} = -\frac{\hbar}{2m} \cdot \nabla^2 \psi_{imag}(r,t) + \frac{1}{\hbar} V\psi_{imag}(r,t), \tag{3 a}$$

$$\frac{\partial \psi_{imag}(r,t)}{\partial t} = \frac{\hbar}{2m} \cdot \nabla^2 \psi_{real}(r,t) - \frac{1}{\hbar} V\psi_{real}(r,t). \tag{3 b}$$

We begin by assuming a two-dimensional space. We write $\psi^n(i,j) = \psi(i \cdot \Delta x, j \cdot \Delta x, n \cdot \Delta t)$ where i, j, and n are indices and Δx and Δt are the spatial and temporal steps, respectively. (The same spatial interval Δx is used in both the x and y directions.) Starting with Eq. (3a), the finite-difference approximations in space and time result in

$$\frac{\psi^n_{real}(i,j) - \psi^{n-1}_{real}(i,j)}{\Delta t}$$

$$= -\frac{\hbar}{2m} \frac{1}{(\Delta x)^2} \left[\begin{array}{c} \psi^{n-1/2}_{imag}(i+1,j) - 4\psi^{n-1/2}_{imag}(i,j) + \psi^{n-1/2}_{imag}(i-1,j) \\ + \psi^{n-1/2}_{imag}(i,j+1) + \psi^{n-1/2}_{imag}(i-1,j-1) \end{array} \right],$$

$$+ \frac{1}{\hbar} V(i,j) \cdot \psi^{n-1/2}_{imag}(i,j)$$

from which we get

4

$$\psi^n{}_{real}(i,j) = \psi^{n-1}{}_{real}(i,j)$$

$$-\frac{\Delta t}{\Delta x^2}\frac{\hbar}{2m}\left[\begin{array}{c}\psi^{n-1/2}{}_{imag}(i+1,j)-4\psi^{n-1/2}{}_{imag}(i,j)+\psi^{n-1/2}{}_{imag}(i-1,j)\\ +\psi^{n-1/2}{}_{imag}(i,j+1)+\psi^{n-1/2}{}_{imag}(i,j-1)\end{array}\right]$$

$$+\frac{\Delta t}{\hbar}V(i,j)\cdot\psi^{n-1/2}{}_{imag}(i,j).$$

The two coupled equations can then be written

$$\psi^n{}_{real}(i,j) = \psi^{n-1}{}_{real}(i,j)$$

$$-\frac{\Delta t}{\Delta x^2}\frac{\hbar}{2m}\cdot\left[\begin{array}{c}\psi^{n-1/2}{}_{imag}(i+1,j)-4\psi^{n-1/2}{}_{imag}(i,j)+\psi^{n-1/2}{}_{imag}(i-1,j)\\ +\psi^{n-1/2}{}_{imag}(i,j+1)+\psi^{n-1/2}{}_{imag}(i,j-1)\end{array}\right], \qquad (4\ a)$$

$$+\frac{\Delta t}{\hbar}V(i,j)\cdot\psi^{n-1/2}{}_{imag}(i,j)$$

$$\psi^{n+1/2}{}_{imag}(i,j) = \psi^{n-1/2}{}_{imag}(i,j)$$

$$+\frac{\Delta t}{\Delta x^2}\frac{\hbar}{2m}\cdot\left[\begin{array}{c}\psi^n{}_{real}(i+1,j)-2\psi^n{}_{real}(i,j)+\psi^n{}_{real}(i-1.j)\\ +\psi^n{}_{real}(i,j+1)+\psi^n{}_{real}(i,j-1)\end{array}\right] \qquad (4\ b)$$

$$-\frac{\Delta t}{\hbar}V(i,j)\cdot\psi^n{}_{real}(i,j).$$

Harmonic Oscillator Simulation

One of the well-known canonical problems in quantum mechanics is the harmonic oscillator. The harmonic oscillator potential is given by [7]

$$V(x,y) = \frac{1}{2}k_0\cdot\left(x^2+y^2\right).$$

In the finite-difference formulation, this is expressed as

$$v(i,j) = \frac{1}{2}k_0\cdot\left[(i-ic)\cdot\Delta x + (j-jc)\cdot\Delta x\right]^2. \qquad (5)$$

It is centered around *(ic, jc)* , the middle of the problem space. The parameter k_0 is

$$k_0 = m\cdot\omega_0{}^2$$

and ω_0, the frequency of oscillation, is related to the ground state energy of the system by

$$E_0 = \hbar\omega_0. \qquad (6)$$

An Electron in a Magnetic Field

This section describes the additional influence of a magnetic field oriented in the z direction. We do this by simulating the vector potential A [7]

$$A = B_0(-y\hat{i} + x\hat{j}),$$ (7)

which gives

$$B = \nabla \times A = 2 \cdot B_0 \, \hat{z}$$

where $\hat{z}$ is a unit vector in the z direction.

The following formalism implements this into the Schroedinger equation:

$$i\hbar \frac{\partial \psi(x,y)}{\partial t} = \frac{1}{2m}\left(\frac{\hbar}{i}\nabla - q \cdot A\right)^2 \psi(x,y) + V(x,y) \cdot \psi(x,y)$$ (8)

$$= \frac{1}{2m}\left(-\hbar^2\nabla^2 - \frac{\hbar}{i}q\nabla A - A\frac{\hbar}{i}q\nabla + q^2 A^2\right)\psi(x,y) + V(x,y)\cdot \psi(x,y).$$

The three A terms used in Eq. (8) are determined by

$$A^2 = B_0^2(y^2 + x^2),$$ (9 a)

$$\nabla A = \left(\hat{i}\frac{\partial}{\partial x} + \hat{j}\frac{\partial}{\partial y}\right) \cdot B_0\left(-y\hat{i} + x\hat{j}\right) = B_0\left(-y\frac{\partial}{\partial x} + x\frac{\partial}{\partial y}\right),$$ (9 b)

$$A\nabla = B_0\left(-y\hat{i} + x\hat{j}\right) \cdot \left(\hat{i}\frac{\partial}{\partial x} + \hat{j}\frac{\partial}{\partial y}\right) = B_0\left(-y\frac{\partial}{\partial x} + x\frac{\partial}{\partial y}\right).$$ (9 c)

Putting these into Eq. (8) results in the following:

$$\frac{\partial \psi(x,y)}{\partial t} = \frac{\hbar^2}{2m\hbar}\left(\frac{d^2}{dx^2} + \frac{d^2}{dx^2}\right)i\psi(rx,y)$$

$$- \frac{B_0^2 q^2(x^2+y^2)}{2m\hbar}i\psi(x,y) + 2\frac{B_0 q}{2m}\left(-y\frac{d}{dx} + x\frac{d}{dy}\right)\psi(rx,y)$$

$$+ V(x,y)\cdot \psi(x,y).$$

Now we take the finite-difference approximations to the spatial and temporal derivatives, along with the formulation of the harmonic oscillator potential of Eq. (5):

6

$$\psi^n_{real}(i,j) = \psi^{n-1}_{real}(i,j)$$

$$- \frac{\hbar}{2m} \frac{\Delta t}{\Delta x^2} \left[\begin{array}{c} -4\psi^{n-1/2}_{imag}(i,j) + \psi^{n-1/2}_{imag}(i+1,j) + \psi^{n-1/2}_{imag}(i-1,j) \\ +\psi^{n-1/2}_{imag}(i,j+1) + \psi^{n-1/2}_{imag}(i,j-1) \end{array} \right]$$

$$+ \frac{B_0^2 q^2}{2m\hbar} \Delta t \left[\Delta x^2 (i-ic)^2 + \Delta x^2 (j-jc)^2 \right] \psi^{n-1/2}_{imag}(i,j) \tag{10}$$

$$+ \frac{B_0 q}{m} \Delta t \left[\begin{array}{c} \Delta x(i-ic) \dfrac{\left(\psi^{n-1}_{real}(i,j+1) - \psi^{n-1}_{real}(i,j-1) \right)}{2\Delta x} \\[2ex] - \Delta x(j-jc) \dfrac{\left(\psi^{n-1}_{real}(i+1,j) - \psi^{n-1}_{real}(i-1,j) \right)}{2\Delta x} \end{array} \right]$$

$$+ \frac{1}{2} k_0 \cdot \left[(i-ic)\cdot\Delta x + (j-jc)\cdot\Delta x \right]^2 \psi^{n-1/2}_{imag}(i,j).$$

Of course, there will be a similar equation corresponding to the imaginary part of ψ.

Calculating the Observables

Two quantities of importance in quantum mechanics are the expected values of the kinetic energy and the potential energy. They are calculated from $\psi(x,y)$ as follows:

Kinetic Energy

The expected value of the kinetic energy is given by

$$\langle T \rangle = \left\langle \psi \left| -\frac{\hbar^2}{2m} \nabla^2 \right| \psi \right\rangle = -\frac{\hbar^2}{2m} \int_{-\infty}^{\infty} \left(\psi^* \nabla^2 \psi \right) dr.$$

The Laplacian operator ∇^2 is approximated by

$$\nabla^2 \psi_{real}(i,j) \cong \frac{1}{(\Delta x)^2} \left[\begin{array}{c} \psi_{real}(i-1,j) - 4\psi_{real}(i,j) + \psi_{real}(i+1,j) \\ +\psi_{real}(i,j-1) + \psi_{real}(i,j+1) \end{array} \right].$$

The kinetic energy in the simulation is calculated by

$$\langle T \rangle = -\frac{\hbar}{2 \cdot m_e} \sum_{j=1}^{N} \sum_{i=1}^{N} \left\{ \left[\psi_{real}(i,j) - i\cdot\psi_{imag}(i,j) \right] \cdot \left[\nabla^2 \psi_{real}(i,j) + i\nabla^2\psi_{imag}(i,j) \right] \right\}. \tag{11}$$

Potential Energy

The expected value of the potential is

$$\langle V \rangle = \langle \psi \,|\, V \,|\, \psi \rangle = \int_{-\infty}^{\infty} V(x,y) |\psi(x,y)|^2 \, dr,$$

which is calculated by

$$\langle V \rangle = \sum_{j=1}^{N} \sum_{i=1}^{N} v(i,j) \cdot \left[\psi^2_{real}(i,j) + \psi^2_{imag}(i,j) \right]. \tag{12}$$

7

III. Determining the Eigenfunctions

The first step in determining the eigenfunctions is to determine the corresponding eigenfrequencies. We do this by initiating the problem with a test function at a point in the problem space and storing the time-domain data at the point of origin of the test. The test function is chosen as a narrow pulse to insure that it will be a superposition of as many of the eigenfunctions as possible. After a sufficient number of time steps (typically about 30,000 to 50,000), the program is halted, and a Fourier analysis of the time domain data collected at the source point is performed. The peaks in the Fourier analysis determine the eigenfrequencies.

Once we determine the eigenfrequencies, the eigenfunctions can be constructed. Because the Fourier analysis resulted in a peak in the Fourier domain, we know that the eigenfunction was present in the original test function. Therefore, by performing another Fourier analysis at every point in the problem space at that frequency, the amplitude and phase of that eigenfunction can be reconstructed.

The Fourier analysis to determine the eigenfrequencies is accomplished by post processing, i. e., an analysis of the data takes place after the simulation is complete at only one data point within the problem space. To construct the eigenfrequencies, however, we need to perform the Fourier analysis everywhere in the problem space, but for a limited number of frequencies. This is done by a discrete Fourier transform (DFT) during the simulation, sometimes referred to as a "running Fourier transform" [4, 5].

To carry out the Fourier analysis at one frequency, say f_1, we could compute the following:

$$\Psi_f = \int_0^{\infty} \psi(t)\, e^{-i2\pi f_1}\, dt. \tag{13}$$

(We take the lower level of integration to be zero because we assume all functions are causal, since we initialize them to zero when the simulation begins.) Taking Eq. (13) into the sampled time domain gives

$$\Psi(n \cdot \Delta t) = \sum_{n=0}^{N} \left[\psi_{real}(n \cdot \Delta t) + i\psi_{f_{imag}}(n \cdot \Delta t) \right] \cdot \left[\cos(2\pi f_1 n \cdot \Delta t) + i\sin(2\pi f_1 n \cdot \Delta t) \right]$$

or

$$\Psi_{f_{real}}(N \cdot \Delta t) = \sum_{n=0}^{N} \left[\psi_{real}(n \cdot \Delta t) \cos(2\pi f_1 \Delta t \cdot n) - \psi_{imag}(n \cdot \Delta t) \cdot \sin(2\pi f_1 \Delta t \cdot n) \right] \qquad \text{(14 a)}$$

$$\Psi_{f_{imag}}(N \cdot \Delta t) = \sum_{n=0}^{N} \left[\psi_{real}(n \cdot \Delta t) \sin(2\pi f_1 \Delta t \cdot n) + \psi_{imag}(n \cdot \Delta t) \cdot \cos(2\pi f_1 \Delta t \cdot n) \right]. \qquad \text{(14 b)}$$

Two equations like (14 a) and (14 b) are needed for every frequency of interest. They are calculated at every cell in the problem space. This is made possible by noticing that the summation in Eq. (14a), for instance, can be calculated by the following simple equation while the simulation program is running:

$$\Psi_{f_{real}}(N \cdot \Delta t) = \Psi_{f_{real}}(N - 1 \cdot \Delta t)$$
$$+ \left(\psi_{real}(n \cdot \Delta t) \cos(2\pi f_1 \Delta t \cdot n) - \psi_{imag}(n \cdot \Delta t) \cdot \sin(2\pi f_1 \Delta t \cdot n) \right).$$

At every point N, the new value is calculated by adding one more term to the value at N-1.

When the program has run for a sufficient length of time, the results of Eq. (14 a) and (14.b) are used to calculated the amplitude and phase at that frequency. These are used to reconstruct the time-domain eigenfunctions. This process is illustrated in Fig. 1. Note that there is one optional step indicated by the dashed line. Once the eigenfunctions have been determined, one of them can be used to initialize the FDTD program. This is useful to insure that it is indeed an eigenfunction that remains stable.

IV. Determining the Eigenfunctions of a Harmonic Oscillator Potential

In this section, we will determine the eigenfunctions and eigenvalues of a harmonic oscillator potential. This is a problem with an analytic solution which provides a check of the accuracy of the method. We will use a two-dimensional harmonic oscillator potential with a ground state energy of 2 meV. The cells in the simulation program are 5 nanometers (nm) and the time steps are 0.1 femtoseconds [Δx and Δt, respectively, in Eq. (10)]. The problem space is 50x50, effectively modeling an area which is 250x250 nm. We begin by initializing the problem with a test function in the middle of the problem space (Fig. 2). This is a Gaussian pulse with an envelope of 15 nm. Note the values of kinetic and potential energy, as calculated by Eq. (11) and (12). Since this test particle is sitting on the bottom of the potential, it initially has very little potential energy. After 2000 iterations, or 0.2 picoseconds (ps), the wave function has begun to expand outward. It has exchanged some of its kinetic energy for potential energy, but the total energy remains the same. The waveform continues oscillating in and out.

After 50,000 iterations (5 ps), the simulation is halted. Figure 3 shows the time domain data at the source point. The Fourier transform of this data is shown in Fig. 4a. The first few peaks occur at 2, 6, 10, and 14 meV where frequencies have been converted to energies by multiplication by Planck's constant.

We initiate the FDTD simulation once again with the same test function. However, this time the program takes the discrete Fourier transform at the frequencies corresponding to the above-mentioned energies (0.48, 1.45, 2.42, and 3.39 THz). At the end of the simulation, the Fourier data is used to reconstruct the eigenfunctions shown in Fig. 4 (b).

The two-dimensional harmonic oscillator eigenfunctions can be characterized by the quantum numbers n and l, where n is a positive integer corresponding to the number of nodes in the wave function as one moves out radially from the center, the principle quantum number [1]. The other number l corresponds to angular momentum, and is clearly 0 for all of these functions since they are all radially symmetric. The eigenenergies corresponding to the quantum numbers n, l are

$$E_{n,l} = E_0(2n + |l| + 1), \tag{15}$$

where E_0 is 2 meV for the present case. Given that $l = 0$, the four lowest states correspond to $n = 0, 1, 2,$ and 3, which result in energies of 2, 6, 10, and 14 meV, as we had determined from Fig. 4 a.

That we did not find eigenfunctions for values of l other than zero should not be surprising since we started with a symmetric test function in a symmetric potential. Suppose, however, that we begin with a test function 50 nm from the center and initialize it with a wave function that has a wavelength of 100 nm and a Gaussian envelope of 35 nm (Fig 5). Note that this test function starts with significant potential as well as kinetic energy. As the simulation progresses, the function moves around the potential, maintaining constant values of kinetic and potential energies, since it remains at about a constant level in the potential. After 5 ps, the simulation is halted, and we have the time-domain data at the source point (Fig. 6). After doing a Fourier transform, we have the data of Fig. 7(a). The peak at 2 meV will be the same (n=0, l=0) eigenfunction of Fig. 4(b), so we will run the discrete Fourier transform at 4, 6, 8, and 10 meV. The resulting eigenfunctions are shown in Fig. 7(b). Note that these all have $n = 0$, and positive integer values of l { $2|l|$ is the number of nodes moving circumferentially about the dot

[1]}. The energy values correspond to those calculated by Eq. (15) for $l = 1, 2, 3$, and 4. Obviously, we could run other test functions that would result in mixed values of n and l.

Suppose we have the same problem with a magnetic field of 2 Telsa. The magnetic field has its greatest effect on states with angular momentum, so we will rerun the previous simulation with a particle of wavelength of 100 nm in a Gaussian envelope of 35 nm initialized 50 nm from the center. The resulting time-domain function is similar in form to Fig. 6, but results in the Fourier amplitude of Fig. 8(a). The pattern is the same, but the peaks have been shifted. Specifically, the $l = 1$ state has shifted from 4 meV to 6.7 meV, the $l = 2$ state from 6 to 10.9 meV, etc. In fact, these are the energy levels predicted from [1]:

$$E_{n,l} = \left[l\hbar\omega_c / 2 + \sqrt{(\hbar\omega_c / 2)^2 + E_o^2 (2n + |l| + 1)} \right], \qquad (16)$$

where ω_c, is the cyclotron frequency,

$$\omega_c = \frac{eB}{m}. \qquad (17)$$

{For m in Eq. (17), we use the reduced mass of an electron in GaAs [1].} The resulting eigenfunctions in Fig. 9(b) are similar to those in Fig. 7(b), except they are slightly closer to the center, which results from the additional confinement imposed by the B field.

V. Eigenfunctions of a Stadium Potential

In this section we will use the same method to find eigenfrequencies and functions of a configuration whose values and functions are not previously known. We will use the "stadium" potential [8] illustrated in Fig. 9. This has a ground potential of 0; the stadium is shaped by a potential barrier of 1 eV. As long as the test functions are on the order of meV, we have almost complete containment.

We begin by initializing a test function at point A and letting the simulation run for 30,000 iterations. We then take the Fourier transform of the time domain data collected at the source, which results in the spectrum shown in Fig. 10a. From this, we ascertain that there are eigenfrequencies at 0.31, 0.88, 1.79, and 2.9 meV. When we rerun the simulation computing the discrete Fourier transform at these frequencies, we obtain the functions of Fig. 10(b). Note that we have obtained eigenfunctions that are symmetric in both directions. This is not surprising, since our test function started from the middle of the stadium.

In order to look for other eigenfunctions, we repeat the simulation by initializing the test function at point B, which results in the frequency response shown in Fig. 11a. The lowest peak is at 0.31 meV; this is obviously the ground state illustrated in Fig. 10, so there is no sense redoing this one. We take the next frequencies which are 1.05, 1.67, 2.25, and 2.87 meV. The result is the functions shown in Fig. 11b.

In order to convince ourselves that these truly are eigenfunctions, we can use them to initialize the simulation. We will take the eigenfunction at 2.87 meV. Using this, the simulation was repeated, as illustrated in Fig. 12. As the simulation progresses, there is movement in the function; but at 1.45 picoseconds, it has returned to its original form. The revival time, calculated by the inverse eigenfrequency

$$T_{revival} = \frac{\hbar}{E} = \frac{4.14 \times 10^{-15} \text{ eV} \cdot \text{sec}}{.00283 \text{ eV}} = 1.46 \times 10^{-12} \text{ sec}, \tag{18}$$

predicts this. One can also verify that $|\psi(t)|^2$ is independent of time.

VI. Discussion

We have described and demonstrated a simulation technique to determine the eigenfunctions for arbitrary nanostructures. The simulation is based on the finite-difference time-domain (FDTD) method. The strength of this method is its flexibility; there is no limit to the complexity of the potential of the structure being simulated, other than what can be accommodated by the discretization. This method is also capable of simulating the influence of a magnetic field. The accuracy of the method was demonstrated by simulating a two dimensional harmonic oscillator with and without the magnetic field. The expected energy values and eigenfunctions were obtained. The full flexibility of the method was demonstrated by finding the eigenfunctions of a stadium-shaped potential.

This technique is powerful enough to study the dynamics in systems where the time dependence plays a central role, such as for wavepackets or in the presence of time-dependent fields. In the future, we will show that the technique may also be generalized in a straightforward way to deal with few-electron wavefunctions in quantum dots within the Hartree-Fock approximation.

Acknowledgements

REFERENCES

1. R. C. Ashoori, Electrons in artificial atoms, *Nature*, **379**, 413 (1996).

2. A. Taflove, *Computational Electrodynamics--the Finite-Difference Time-Domain Method.*, (Artech House, Boston, MA, 1995).

3. D. Sullivan, *Electromagnetic Simulation Using the FDTD Method.* (IEEE Press,New York 2000).

4. C. M. Furse, S. P. Mathur, and O. P. Gandhi, Improvements to the finite-difference time-domain method for calculating the radar cross section of a perfectly conducting target, *IEEE Trans. Microwave Theory and Tech.*, **38**, 919 (1990).

5. D. M. Sullivan, Mathematical methods for treatment planning in deep regional hyperthermia, *IEEE Trans. Microwave Theory and Tech.*, **39**, 864 (1991).

6. J. Jacak, P. Hawrylak, and A. Wojs, *Quantum Dots*, Springer, Berlin 1997).

7. C. Cohen-Tannoudji, B. Diu, and F. Laloe, *Quantum Mechanics.* (John Wiley and Sons, New York (1977).

8. S. Tomsovic and E. J. Heller, Long-time semiclassical dynamics of chaos: the stadium billiard, *Physics Review E*, **47**, 282 (1993).

Figure Captions

Figure 1   Block diagram for the procedure used to determine the eigenfunctions of an arbitrary quantum nanostructure.

Figure 2   Time-domain evolution of the testing function initiated at the center of the two-dimensional harmonic oscillator potential. The original testing function is a Gaussian envelope of 3 nm. Note that the total energy of the function remains constant, but there is an exchange between kinetic and potential energy. (Only the real part of the wavefunction is shown.)

Figure 3   Time-domain data sampled at the source point for the simulation illustrated in Fig. 2.

Figure 4   (a) Fourier analysis of the time-domain data of Fig. 3, (b) Eigenfunctions reconstructed via the DFT at the eigenfrequencies found in (a).

Figure 5   Time-domain evolution of the testing function initiated 50 nm from the center of the harmonic oscillator potential. This function was initiated as a waveform with a wavelength of 100 nm inside a Gaussian envelope of 35 nm, giving it substantial kinetic energy. (Only the real part of the wavefunction is shown.)

Figure 6   Time-domain data sampled at the source point for the simulation illustrated in Fig. 5.

Figure 7   (a) Fourier analysis of the time-domain data of Fig. 6,   (b) Eigenfunctions reconstructed via the DFT at the eigenfrequencies found in (a).

Figure 8   (a) Fourier analysis of the time-domain data collected for a test function moving in a magnetic field of 2 Telsa. Note that the form of the Fourier analysis is very similar to Fig. 7a, but the peaks are shifted. (b) Eigenfunctions reconstructed via the DFT at the eigenfrequencies found in (a).

Figure 9   Diagram of a "stadium" potential. The inside of the stadium is at zero potential, while the outside is 1 eV.

Figure 10   (a) Fourier analysis of the time-domain data at source point A for the potential illustrated in Fig. 9,   (b) Eigenfunctions reconstructed via the DFT at the eigenfrequencies found in (a).

Figure 11   (a) Fourier analysis of the time-domain data at source point B of Fig. 9 for a testing function initiated at source point B. (b) Eigenfunctions reconstructed via the DFT at the eigenfrequencies found in (a).

Figure 12   Time evolution of a function in the stadium potential that was initiated from the 2.87 meV eigenfunction of Fig. 11b.
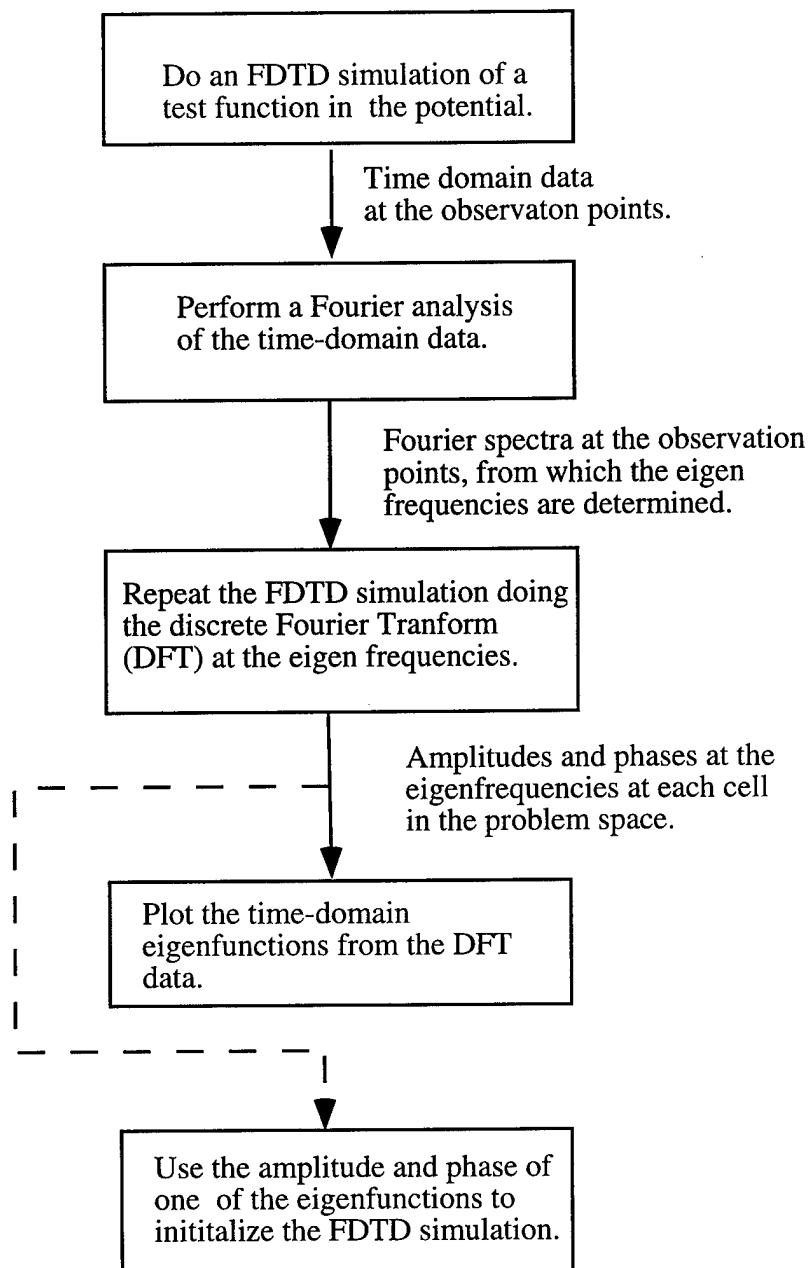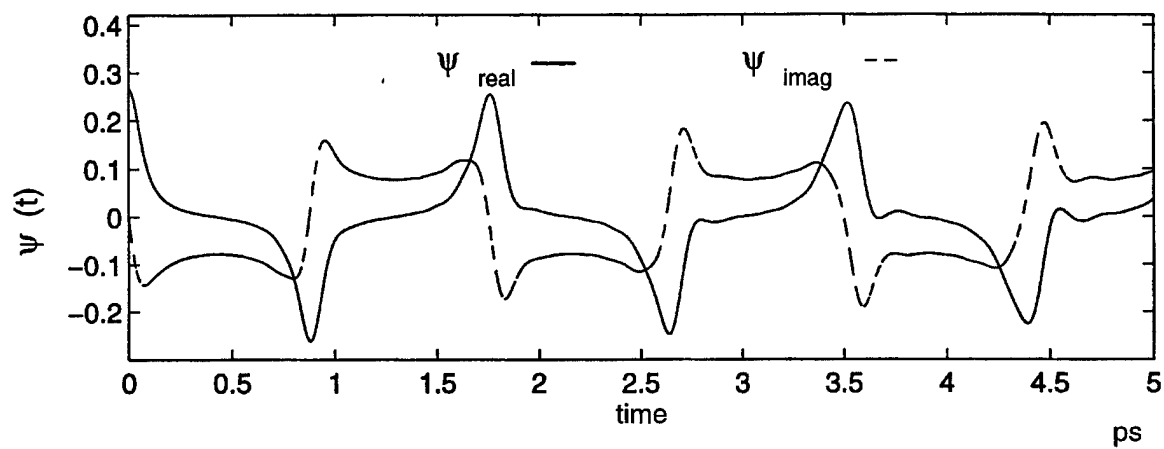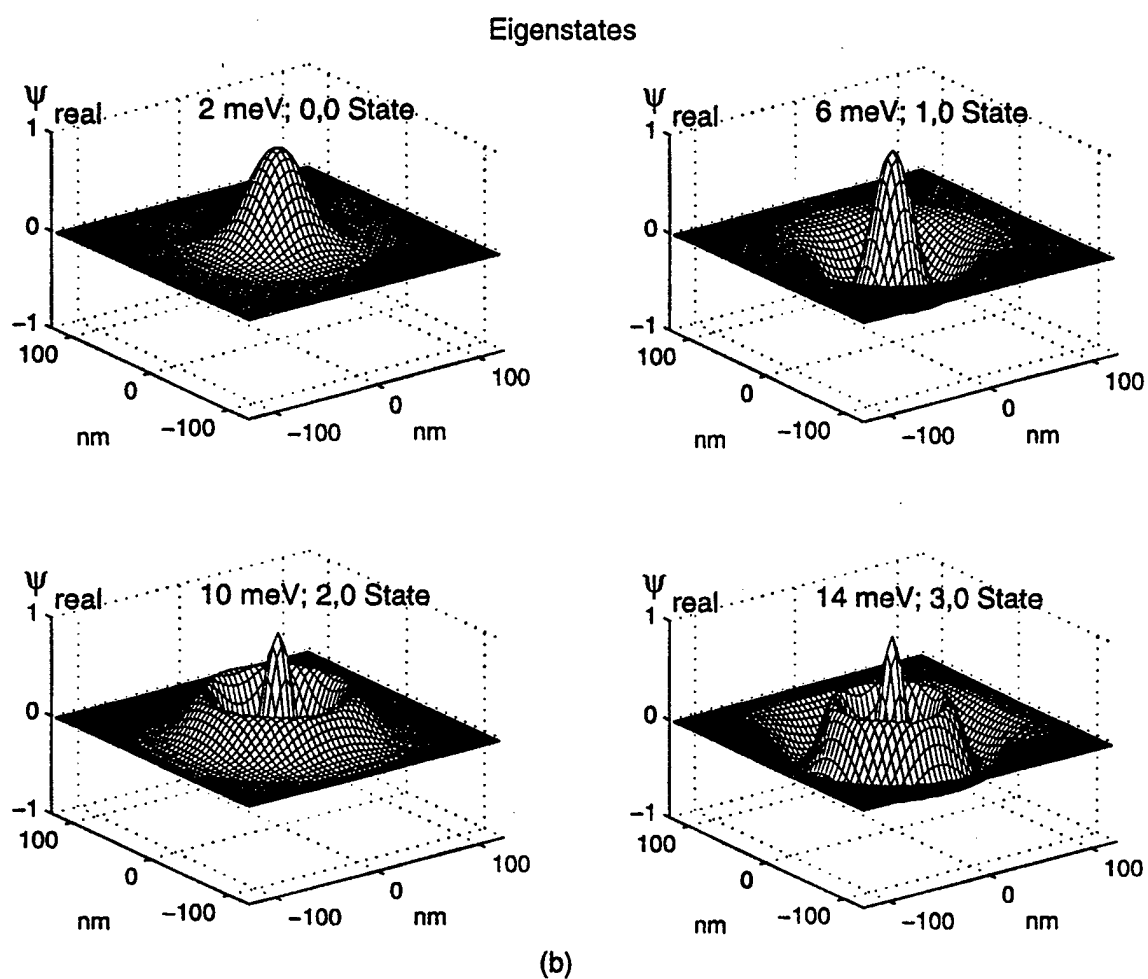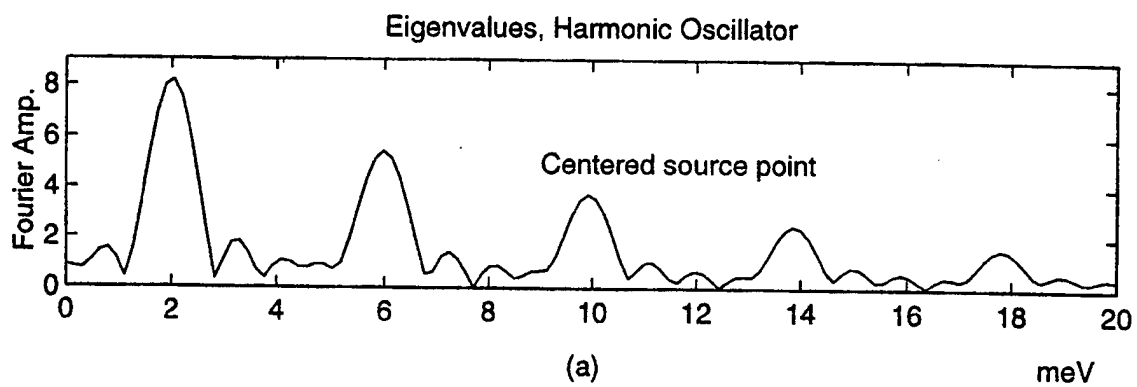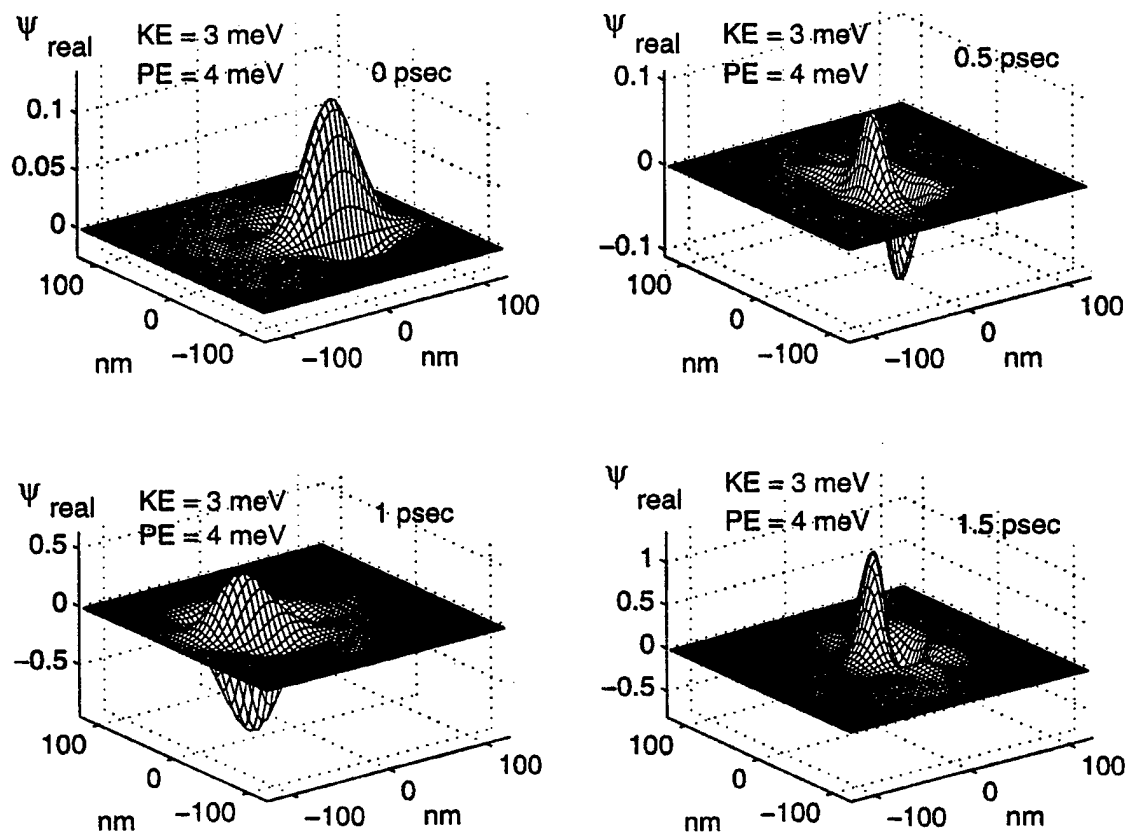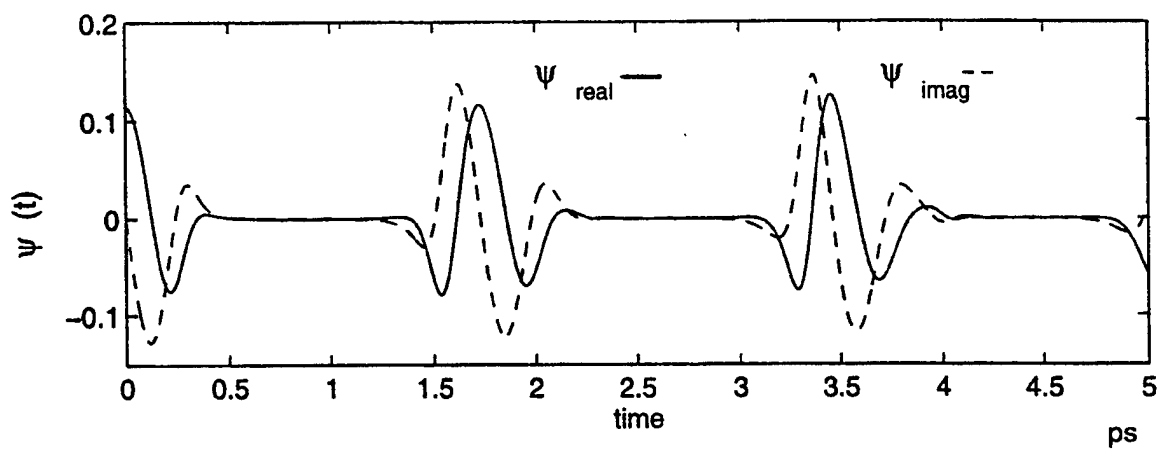
```
┌─────────────────────────────┐
│  Do an FDTD simulation of a │
│  test function in  the      │
│  potential.                 │
└─────────────────────────────┘
              │  Time domain data
              │  at the observaton points.
              ▼
┌─────────────────────────────┐
│  Perform a Fourier analysis │
│  of the time-domain data.   │
│                             │
└─────────────────────────────┘
              │   Fourier spectra at the observation
              │   points, from which the eigen
              │   frequencies are determined.
              ▼
┌─────────────────────────────┐
│ Repeat the FDTD simulation  │
│ doing the discrete Fourier  │
│ Tranform (DFT) at the eigen │
│ frequencies.                │
└─────────────────────────────┘
              │   Amplitudes and phases at the
              │   eigenfrequencies at each cell
              │   in the problem space.
              ▼
┌─────────────────────────────┐
│  Plot the time-domain       │
│  eigenfunctions from the    │
│  DFT data.                  │
└─────────────────────────────┘

              ▼
┌─────────────────────────────┐
│  Use the amplitude and      │
│  phase of one  of the       │
│  eigenfunctions to          │
│  inititalize the FDTD       │
│  simulation.                │
└─────────────────────────────┘
```

Figure 1. Block diagram of the procedure used to determine the eigenfunctions of an arbitrary quantum nanostructure.
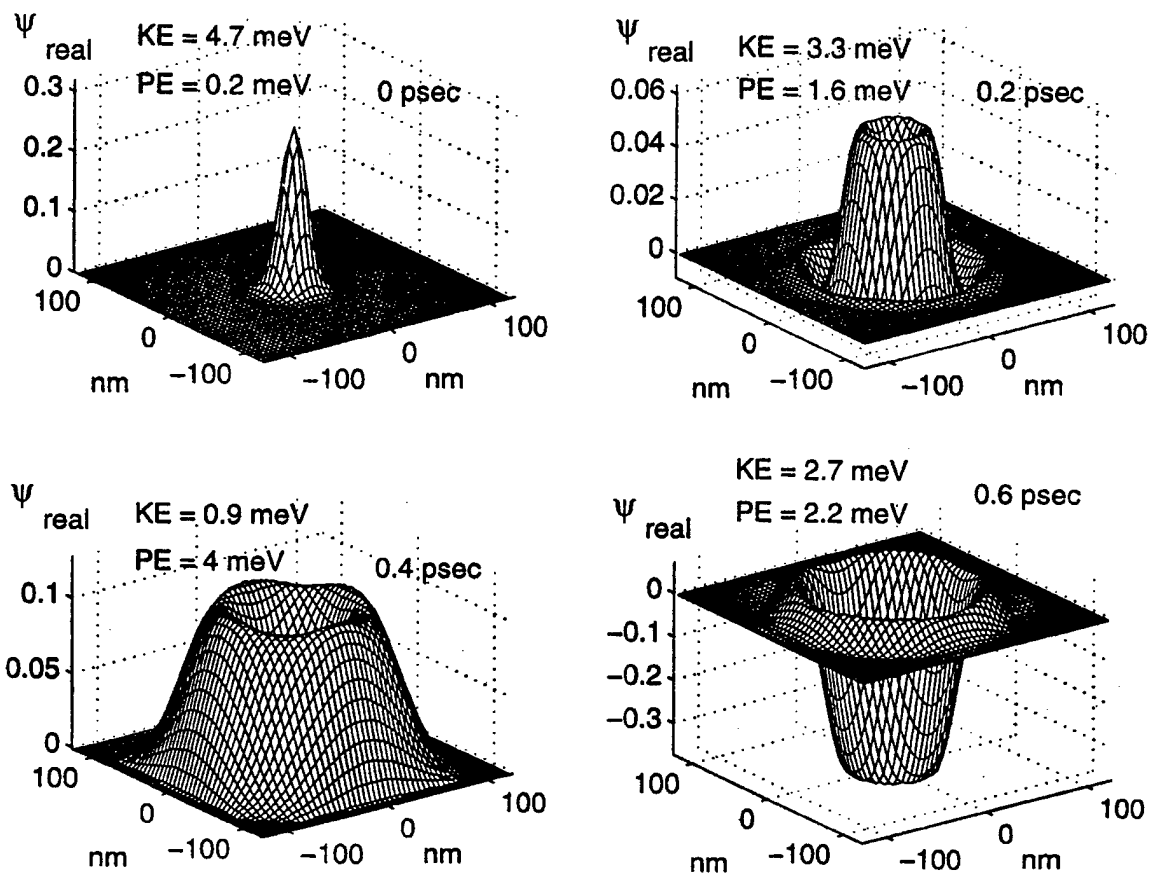
Figure 2. Time-domain evolution of the testing function initiated at the center of the two-dimensional harmonic oscillator potential. The original testing function is a Gaussian pulse of 15 nm. Note that the total energy of the function remains constant, but there is an exchange between kinetic and potential energy. (Only the real part of the wavefunction is shown.)

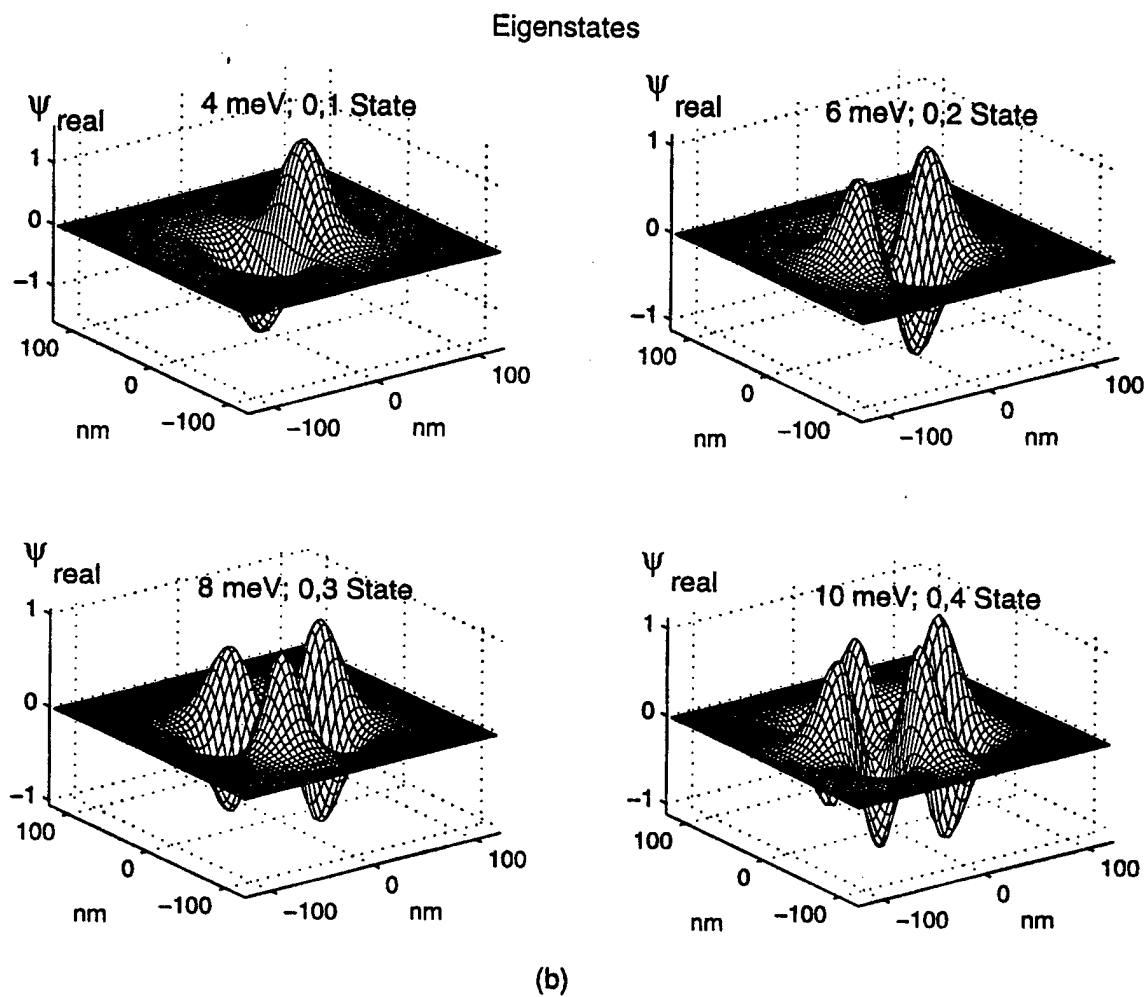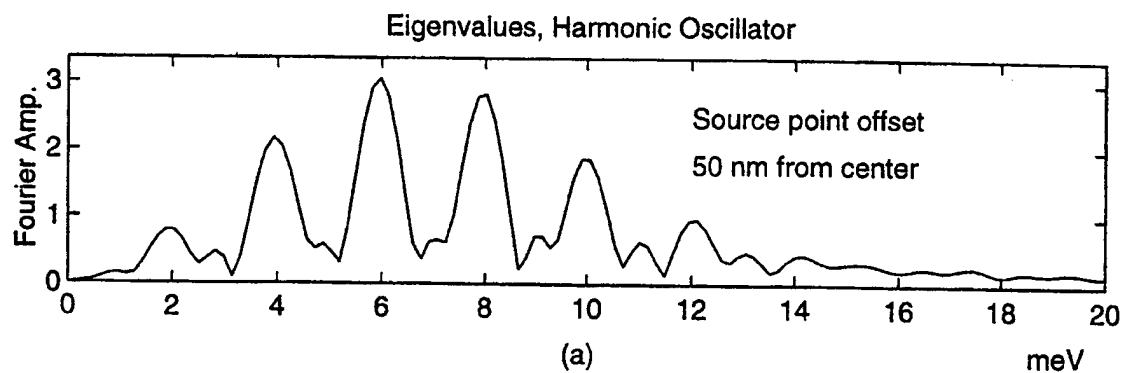Figure 3. Time-domain data sampled at the source point for the simulation illustrated in Fig. 2.

Eigenvalues, Harmonic Oscillator

(a)

Eigenstates

(b)
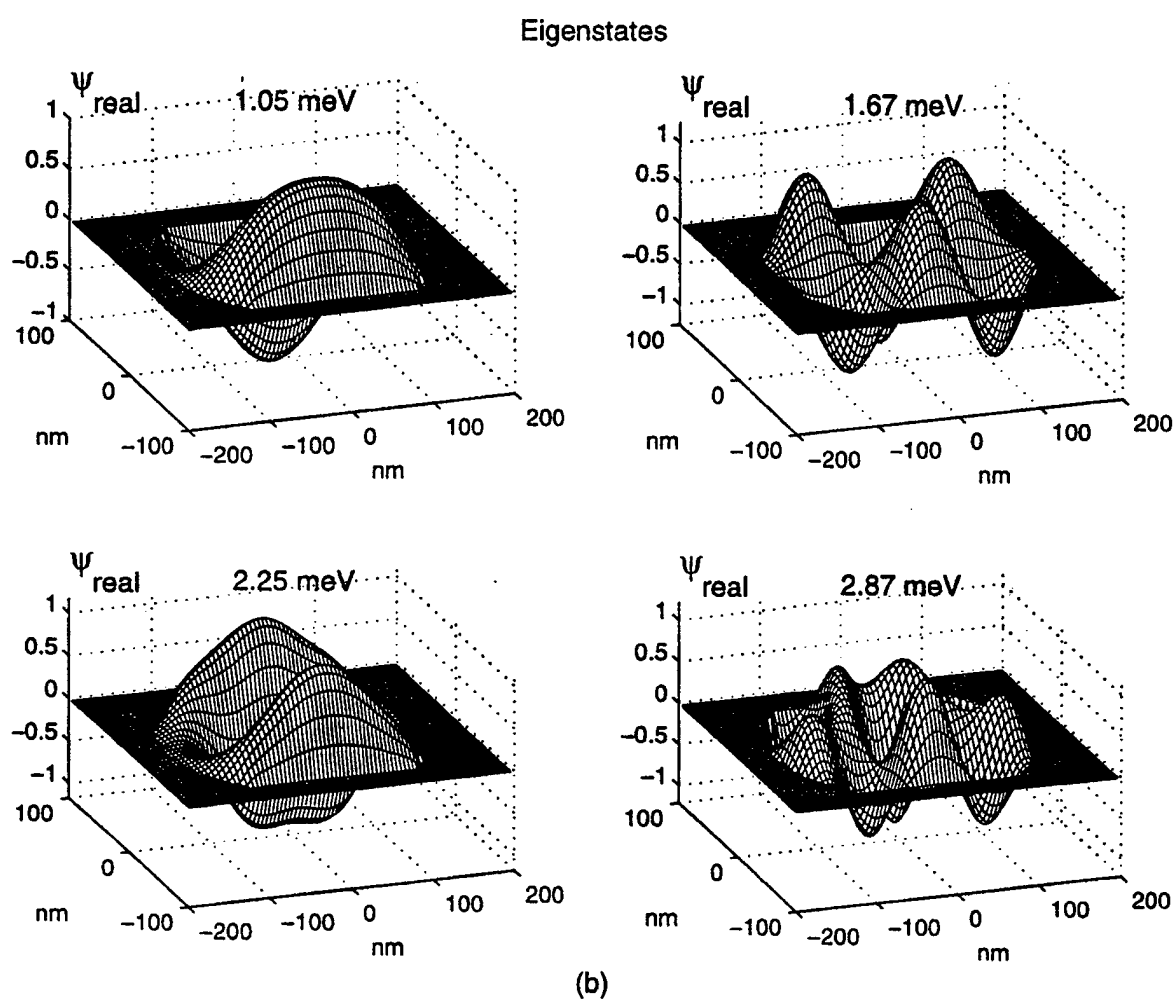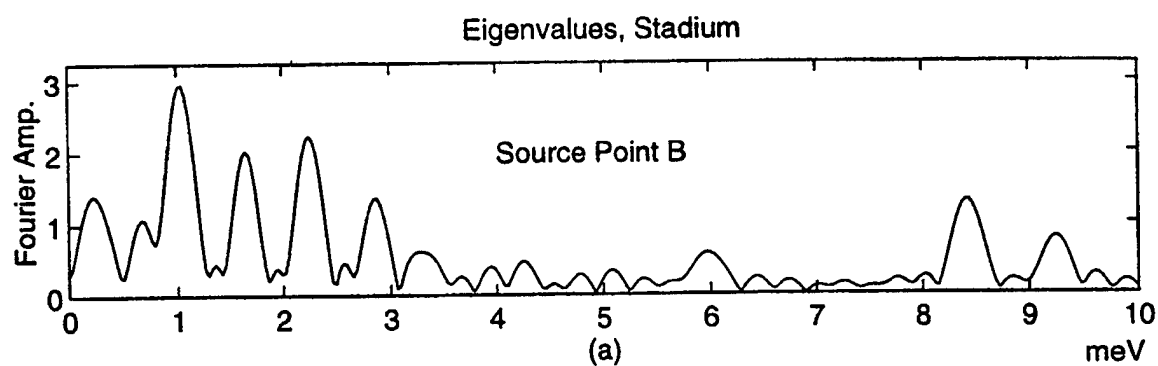
Figure 4. (a) Fourier analysis of the time-domain data of Fig. 3; (b) Eigenfunctions reconstructed via the DFT at the eigenfrequencies found in (a).

Figure 5. Time-domain evolution of the testing function initiated 50 nm from the center of the harmonic oscillator potential. This function was initiated as a waveform with a wavelength of 100 nm inside a Gaussian envelope of 35 nm, giving it substantial kinetic energy. (Only the real part of the wavefunction is shown.)

Figure 6. Time-domain data sampled at the source point for the simulation illustrated in Fig. 5.

Figure 7. (a) Fourier analysis of the time-domain data of Fig. 6; (b) Eigenfunctions reconstructed via the DFT at the eigenfrequencies found in (a).

**Eigenvalues, Harmonic Oscillator with B = 2 T**

Centered source point

Eigenstates

ψ real   6.7 meV

ψ real   10.9 meV

ψ real   15.2 meV

ψ real   19.2 meV

(b)

Figure 8. (a) Fourier analysis of the time domain collected for a test function moving in a harmonic oscillator with a magnetic field of 2 T. Note that the form of the Fourier analysis is very similar to Fig. 7a, but the peaks are shifted. (b) Eigenfunction reconstructed via the DFT at the eigenfrequencies found in (a).
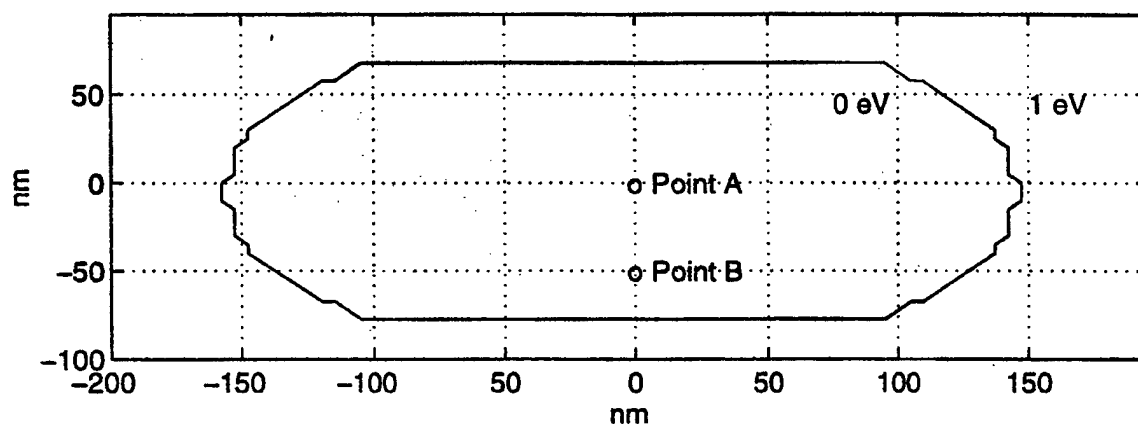
Figure 9. Diagram of a "stadium" potential. The inside of the stadium is at zero potential, while the outside is at 1 eV.
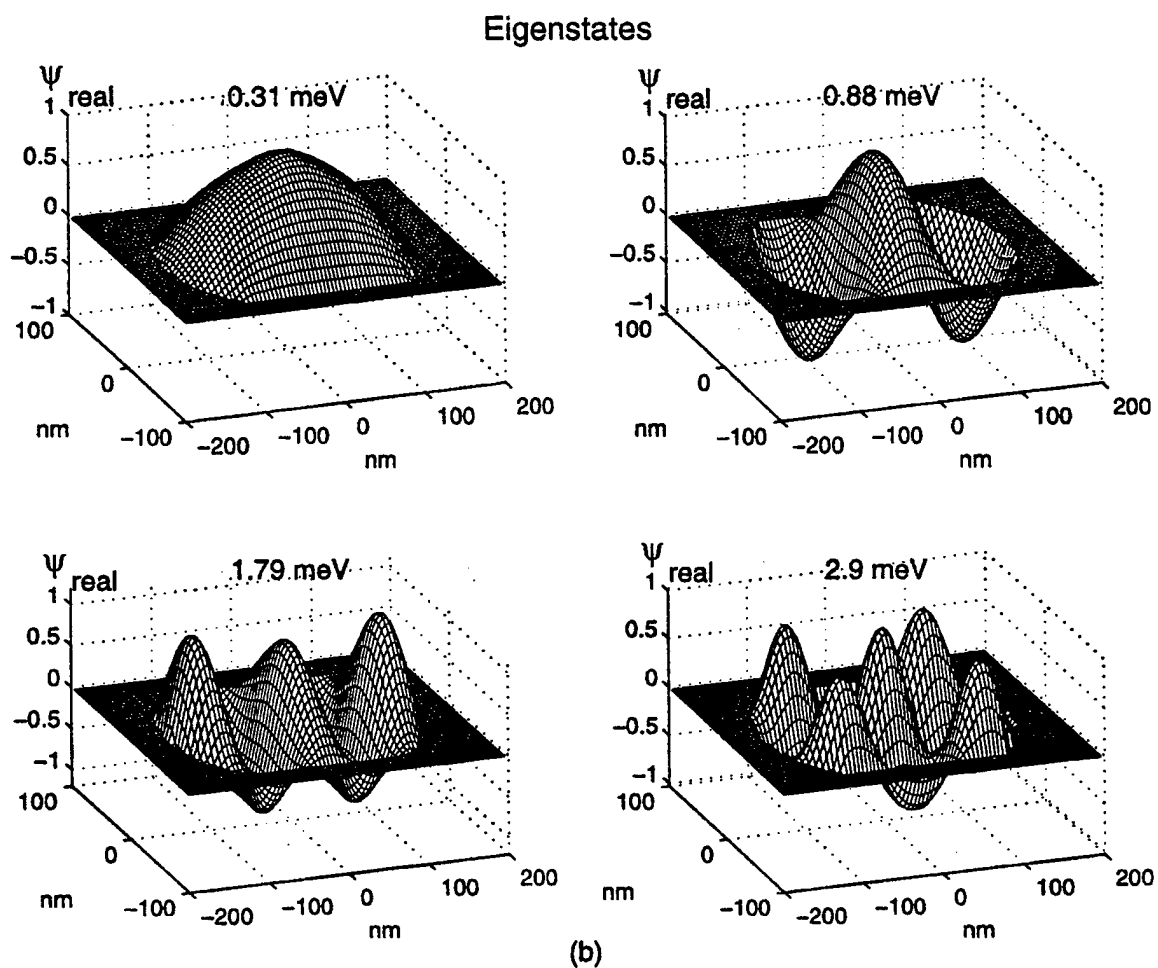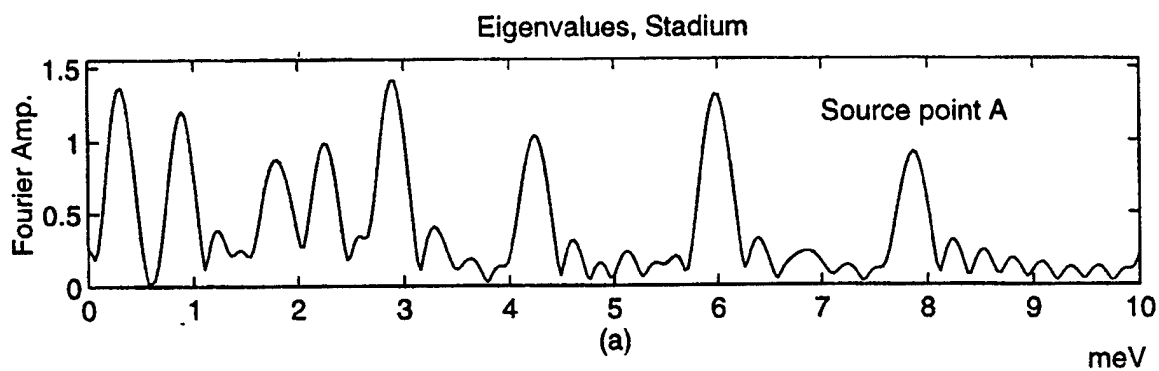
Eigenvalues, Stadium

(a)

meV

Eigenstates

(b)

Figure 10. (a) Fourier analysis of the time-domain data at source point A for the potential illustrated in Fig. 9; (b) Eigenfunctions reconstructed via the DFT at the eigenfrequencies found in (a).

Figure 11. (a) Fourier analysis of the time-domain data at the source point B of Fig. 9; (b) Eigenfunctions reconstructed via the DFT at the eigenfrequencies found in (a).
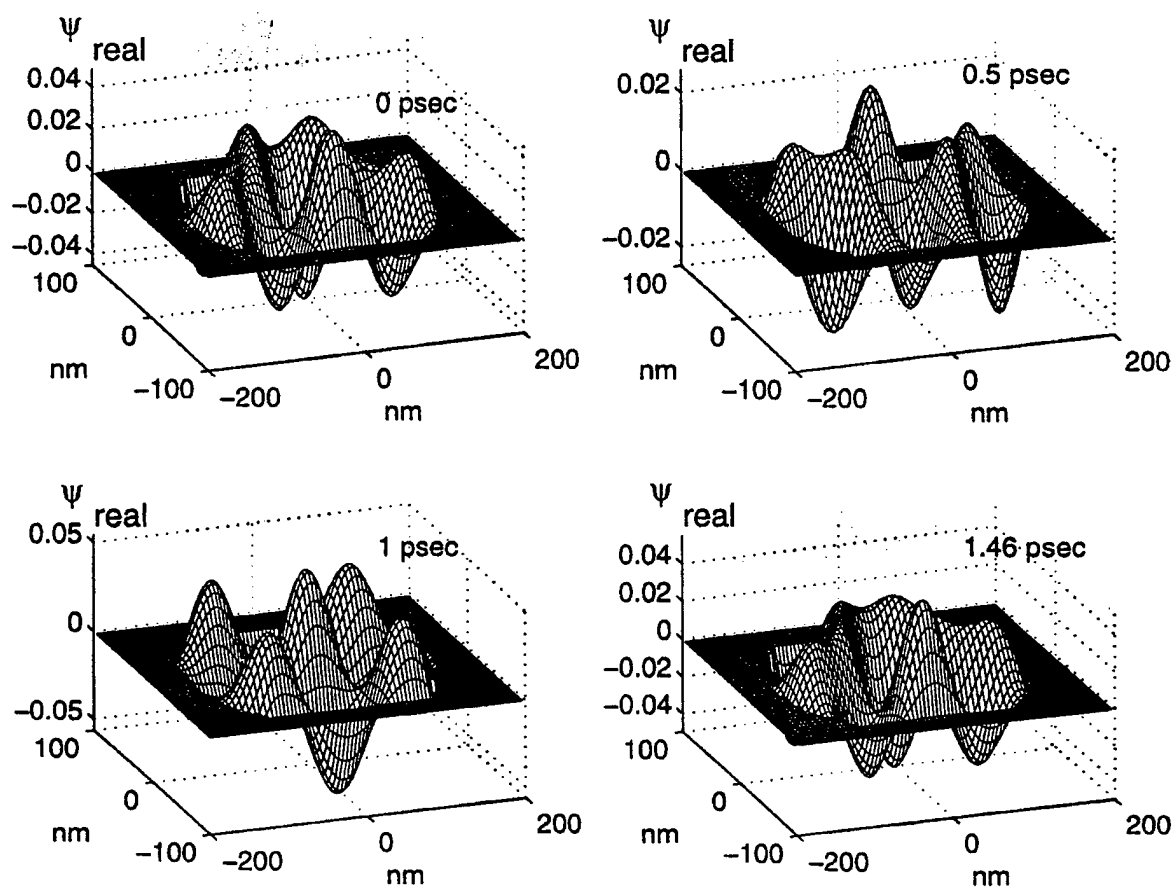
Figure 12. Time evolution of a function in the stadium potential that was initiated from the 2.87 meV eigenfunction of Fig. 11b.

Simulation of Spatiotemporal Terahertz Pulse Shaping in 3-D Using Conductive Apertures of Finite Thickness

Sunil Nekkanti, M. S., Dennis Sullivan, Ph. D.*
Department of Electrical and
Computer Engineering
University of Idaho
Moscow, Idaho 83844-1023
(208) 885-5926
dennis@ee.uidaho.edu

D. S. Citrin, Ph.D.
Department of Physics
and Materials Research Center
Washington State University
Pullman, WA 99164-2814
(509) 335-3698
citrin@wsu.edu

* To whom correspondence should be addressed

Abstract

The need for short, high-frequency pulses for spectoscopy and imaging has motivated the search for methods to shape these pulses. Conductive apertures are often used for spatiotemporal shaping of THz pulses. Computer simulation can facilitate the design of such apertures by allowing one to evaluate different configurations and their related parameters. Three-dimensional simulations using the FDTD method with techniques described here make this possible without the need for extraordinary computer resources. The accuracy of this method is confirmed by comparison with previously published experimental data. The versatility of the method is demonstrated by the simulation of apertures of various shapes and sizes.

1. Introduction

Over the past few years, terahertz ($10^{-12} s^{-1}$) technology has been experiencing explosive growth. The growth in this area has been fueled largely by the need for faster signal processing and communications, for high-resolution spectroscopy, atmospheric and astrophysical remote sensing, and for imaging. A number of methods for the generation of THz radiation have been developed. Many of these methods use a photoconductive antenna in which an ultrashort optical pulse is incident upon a strongly biased semiconducting material [1]. Other methods use heterostructures, such as p-i-n junctions [2] and strained superlattices [3]. Some of the applications using these radiated THz pulses require a pulse with a specific shape to improve the prospects for optical control over material behavior and structure. A method for spatiotemporal shaping of the THz pulses by a diffraction through conductive apertures in a two-dimensional space has recently been reported [4]. Simulation of the THz pulse shaping is desirable because it gives an opportunity to find the kind of pulse shape that can be obtained using different apertures. Simulation also allows the investigation of the influence of variations in the parameters much faster and more efficiently than experimental methods.

This paper investigates the effects of the apertures in a three-dimensional problem space. Three-dimensional simulation is more desirable than two-dimensional simulation for three primary reasons. First, the shape in the third dimension can be varied. Second, it is desirable to observe the simulated pulse anywhere in the three-dimensional space and not just be limited to the single horizontal plane provided by a two-dimensional simulation. Third, the wave physics of a two-dimensional space is different from that of one- and three- dimensions [5]. In one- and three-dimensional waves, the shape of the wave is preserved as it travels from its initial position, whereas in a two-dimensional wave there exists a "wake" that trails off after the pulse as it travels forward in time.

To simulate the far field of the aperture in a three-dimensional problem space, prohibitively large amounts of core computer memory would normally be required. To

overcome this, a transformation is used to determine the far field from the near field in the aperture. Furthermore, the problem space can be reduced by exploiting symmetry.

2. Simulation Methods

2.1 The Finite-Difference Time-Domain Method

The finite-difference time-domain (FDTD) method [6]-[8] is one of the most popular numerical methods for solving problems in electromagnetics. The time-domain Maxwell's equations in free space are given by

$$\frac{\partial E}{\partial t} = \frac{1}{\varepsilon_0} \nabla \times H \tag{1 a}$$

$$\frac{\partial H}{\partial t} = -\frac{1}{\mu} \nabla \times E. \tag{1 b}$$

The FDTD formulation implements these as difference equations, two of which are

$$E_x^{n+1/2}(i,j,k+1/2) = E_x^{n-1/2}(i,j,k+1/2)$$
$$+ \frac{\Delta t \cdot c_0}{\Delta x} \left[\begin{array}{l} H_y^n(i+1/2,j,k+1/2) - H_y^n(i-1/2,j,k+1/2) \\ -H_x^n(i,j+1/2,k+1/2) + H_x^n(i,j-1/2,k+1/2) \end{array} \right] \tag{2 a}$$

$$H_z^{n+1}(i+1/2,j+1/2,k) = H_z^n(i+1/2,j+1/2,k)$$
$$+ \frac{\Delta t \cdot c_0}{\Delta x} \left[\begin{array}{l} E_y^n(i+1,j+1/2,k) - E_y^n(i,j+1/2,k) \\ -E_x^n(i+1/2,j+1,k) + E_x^n(i+1/2,j,k) \end{array} \right]. \tag{2 b}$$

Similar equations follow for E_x, E_y, H_x, and H_y fields.

Figure 1(a) is a diagram of a typical experimental setup for spatiotemporal filtering of THz pulses, and Fig 1(b) shows the region to be simulated. The problem domain must be broken into cells for simulation in the FDTD method. (We use cubes with the same dimension in each direction.) Some thought must be given to the size of the cells. We will be dealing with pulses that have frequency components as high as 1 THz. This corresponds to a wavelength of 300 μm. To maintain accuracy under the simulation conditions that we are using, it is desirable to have a sampling rate of twenty points per wavelength, i. e., a cell size of 15 μm. The high sampling rate reduces the propagation error [6] and also reduces error due to the "staircasing"

effect that occurs when modeling metal objects with edges that do not lie in one of the rectangular directions. This means that to simulate a very small area of 4 mm by 7 mm by 4 mm, a problem space of 200x500x200 cells is required. Implementing an FDTD program of this size would require 400 megawords of core memory in the computer.

To overcome this problem, two techniques can be used: The symmetry of the problem can be utilized to reduce the simulated space to one fourth, and a transformation can be used whereby the far field can be determined by the fields in the aperture, eliminating the need to simulate the far field.

2.2 Symmetry

We use the fourfold symmetry of the aperture to reduce the computational problem space. The four quadrants are symmetric about the x = 0 and y = 0 planes; therefore, only one of the four quadrants is simulated. This technique has been used before in FDTD simulation [9].

2.3 The Near-Field to Far-Field Transformation

The diffracted pulse from the aperture is observed in the radiating far field. To include the far field in our computation, a large amount of computer memory is required; however, by implementing the near-field to far-field transformation described in a previous paper [10], the required computational space is dramatically reduced. In this transformation, the FDTD-computed time domain data at the end of the aperture is used to calculated the far-field values (Fig. 2). A brief description follows.

We start with the vector potential

$$A = \frac{1}{4\pi} \iint_S J_s(r') \frac{e^{-jkR}}{R} ds'$$ (3)

where $R = |\bar{r} - \bar{r}'|$. The H field due to the electric current density J is obtained by

$$H = \nabla_r \times A$$

$$= \frac{1}{4\pi} \nabla_r \times \int_V J_s(r') \frac{e^{-jkR}}{R} dv' \tag{4}$$

$$= \frac{1}{4\pi} \int_V (J_s(r') \times \hat{r}) \left(jk + \frac{1}{R} \right) \left(\frac{e^{-jkR}}{R} \right) dv'$$

where $\hat{r} = r_x \hat{x} + r_y \hat{y} + r_z \hat{z} = \dfrac{R}{|R|}$ and $|R| = \left[(x-x')^2 + (y-y')^2 + z^2 \right]^{1/2}$. Using the duality principle,

the E field due to the magnetic current density M is given by

$$E = \frac{-1}{4\pi} \iint_V (M(r') \times \hat{r}) \left(jk + \frac{1}{R} \right) \frac{e^{-jkR}}{R} dv'. \tag{5}$$

For an x-polarized incident plane wave, the direction normal to the aperture is the z direction, so

$$M = 2E_a \times \hat{n}$$
$$= 2E_a \hat{x} \times \hat{z} = -2E_a \hat{y}, \tag{6}$$

where E_a is the field in the aperture. Hence,

$$E = \frac{1}{4\pi} \iint_{apper.} (2E_a(r')\hat{y} \times \hat{r}) \left(jk + \frac{1}{R} \right) \frac{e^{-jkR}}{R} dS' \tag{7}$$

and

$$\hat{y} \times \hat{r} = (r_x \hat{z} - r_z \hat{x}). \tag{8}$$

Therefore, the x-polarized E field is given by

$$E = \frac{1}{2\pi} \iint_{aper.} r_z E_a(r') jk \frac{e^{-jkR}}{R} dS' + \frac{1}{2\pi} \iint_{aper.} r_z E_a(r') \frac{e^{-jkR}}{R^2} dS'. \tag{9}$$

Taking this into the sampled time domain, we get the following equation:

$$E_x^n(i,j,k) \cong \frac{1}{\pi} \sum_i \sum_j r_z \frac{del\_E_a^n(i',j',n-2 \cdot R_{\Delta x})}{R_{\Delta x}}$$
$$+ \frac{1}{2\pi} \sum_i \sum_j r_z \frac{E_a^n(i',j',n-2 \cdot R_{\Delta x})}{R^2_{\Delta x}} \tag{10}$$

where $E_a^n(i',j',n-2 \cdot R_{\Delta x})$ is the time-retarded field at the end of the aperture, and

$$del\_E_a{}^n(i',j',n-2\cdot R_{\Delta x}) = E_a{}^n(i',j',n-1-2\cdot R_{\Delta x}). \qquad (11)$$

More details are given in [10].

Since symmetry is being used, for every point in the plane at the end of the aperture, there exist three other points in the other three quadrants that must be considered to obtain the true transformation. As can be seen from Fig. 3, the point P_1, which is in the simulated quadrant, has symmetry points P_2, P_3, and P_4. The E field values in the aperture at the four points are the same, but the distances to the far-field observation point to each of these four symmetric points is not the same. Hence, when implementing the transformation along with the symmetry, this has to be taken into account.

Using the two techniques described above, we reduce the sample problem that required a domain of 200x400x200 cells to a domain of 100x200x100 cells that requires only 26 megawords of core computer memory. The simulated problem domain is shown in Fig. 4. The near-field to far-field transformation reduces the problem space to a small area around the aperture, and the use of symmetry further reduces the problem space by seventy-five percent. Note that every side of the problem space, except the symmetry planes, has a twelve cell perfectly matched layer (PML) to absorb outgoing scattered waves [11].

3. Verification

To verify the accuracy of the results obtained from the three-dimensional simulation using the symmetry and the transformation techniques, we compare the resulting pulses from the full FDTD simulation with those obtained using the transformation techniques. A Gaussian pulse with a spread of 0.375 picoseconds (or 15 time steps) is diffracted through a rectangular aperture of thickness 1.00 mm and width of 0.5 mm. Comparisons are made at selected points [Fig. 1(b)]. Figures 5(a) and 5(b) show the comparison on-axis at distances of 0.24 mm and 1.5 mm respectively from the aperture. Figures 6(a) and 6(b) show the comparison at off-axis distances of 0.45 mm in the y-direction and x-direction, respectively.

To verify the method against experimental data, we simulate the setup described by Bromage, et al [4], who generated an incident pulse by the illumination of a GaAs wafer with a Ti:sapphire laser operating at 810 nm. The resulting pulse is shown in Fig. 7(a). This was filtered by a rectangular aperture of thickness 1.7 mm and a width of 0.5 mm. For comparison, the resulting pulse and the filtering aperture were simulated. The results, shown in Fig. 7(b), are in good agreement. The reconstructed incident pulse in Fig. 7(a) was used for all subsequent simulations in this paper.

4. Aperture Simulation

In this section, we use the three-dimensional simulation program to evaluate the pulse shaping characteristic from different apertures. We begin with a rectangular aperture and evaluate the effects of the various parameters. We then look at other tapered and circular apertures for comparison.

The specific parameters of the rectangular aperture are the thickness (l) in the z direction, the width (d) in the y direction, and the height (h) in the x direction (Fig. 4). All the observation points in this section are at a distance of 7 mm from the aperture. The results for the pulses obtained by varying the thickness and the width of the aperture were found to be in accordance with the results shown in the paper by Bromage, et al. [4]. When $d = 0.5$ mm and $h = 0.15$ mm, we observe that as the thickness increased, considerable pulse shaping occurs (Fig. 8). Furthermore, the ringing increases due to the fact that the aperture acts as a resonating cavity with increasing thickness. Also for l of 0.23 mm and h of 0.15 mm, as the width increases, narrower pulses are obtained as shown in Fig. 9. This is can be explained by the following: for a rectangular waveguide the width d, the cut-off frequency in free space is given by [12]:

$$f_c = \frac{c}{2d}.$$

As the height of the aperture is increased, we found that only the amplitude of the resulting pulse increased.

The three-dimensional capability was particularly useful in simulating shapes that could not adequately be represented in two-dimensions. Now a tapered aperture can be simulated, as shown in Fig. 10. The resulting pulse after passing through a tapered aperture like Fig. 10 is shown in Fig. 11(a). Another simulation used an aperture tapered on both edges; the resulting pulse is shown in Fig. 11(b). The results of the tapered apertures show pulses that die out smoothly without excessive ringing, as opposed to the untapered rectangular apertures.

The use of a circular aperture was also investigated. After a process of varying parameters, similar to the procedure using the rectangular aperture, we found that a conical shaped aperture (Fig. 12) gave the pulse shapes of Fig. 13. These shapes are very appealing, particularly Fig. 13(a), because they present a couple of very smooth cycles without ringing. However, they do nothing to eliminate the secondary pulse.

Which of the above pulses is best depends upon the application. It was our intention to demonstrate the versatility of the method and the wide variety of pulses that can be obtained with various apertures.

5. Conclusion

In this paper, we carried out three-dimensional simulations of THz spatiotemporal pulse shaping. The computations exploit the symmetry of the problem and a transformation that lets one determine the far field from the fields in the aperture. We also demonstrated that three-dimensional simulation provides a more complete description than two-dimensional simulation because three-dimensional simulation allows the simulation of all parameters in a wider variety of structures. Such simulations facilitate the exploration of pulse shapes achievable in complex, though technologically feasible, geometries. In particular, the full vector nature of the simulations allows for the accurate presentation of pulse shapes far from the propagation axis where scalar techniques are known to fail.

References

1. J. Darrrow, B. Hu, X. C. Zhang, and D. Auston, "Subpicosecond electromagnetic pulses from large-aperture photoconducting antennas," *Optics Letters,* Vol. 15. pp. 323, 1990.

2. L. Xu, X. C. Zhang, D. Auston, and B. Jahali, "Terahertz radiation from large aperture Si p-i-n diodes," *Applied Physics Letters*, Vol. 59, pp. 3357, 1991.

3. X. C. Zhang, B. Hu, S. Xin, and D. Auston, "Optically induced femtosecond electromagnetic pulses from GaSb/AlSb strained-layer superlattices," *Applied Physics Letters*, Vol. 57, pp. 753, 1990.

4. J. Bromage, S. Radic. G. Agrawal, C. Stroud Jr, P. Fauchet, and R. Sobolewski, "Spatiotemporal shaping of half-cycle terahertz pulses by diffracton through conductive apertures of finite thickness," *J. Opt. Soc. Am. B*, Vol. 15, pp. 1399, April 1998.

5. P. M. Morse and H. Feschbach, *Methods of Theoretical Physics*. New York: McGraw Hill, Inc., 1953.

6. A. Taflove, *Computational Electrodynamics: The Finite-Difference Time-domain Method*. Norwood, MA: Artech House, 1995.

7. K. Kunz and R. Luebbers, *The Finite-Difference Time-Domain Method for Electromagnetics*. Boca Raton, FL: CRC Press, 1993.

8. D. M. Sullivan, *Electromagnetic Simulation Using the FDTD Method*, New York, IEEE Press, 2000.

9. D. Sullivan, J. Liu, and M. Kuzyk, "Three-dimensional optical pulse simulation using the FDTD method," *IEEE Trans. Microwave Theory Tech.*, Vol. MTT-48, pp 1127-1133, July, 2000.

10. D. Sullivan and J. Young, "Far field time domain calculation from aperture radiators using the FDTD method," *IEEE Trans. Antennas Prop.*, scheduled for publication, Feb. 2001.

11. D. Sullivan, "An unsplit step 3-D PML for use with the FDTD method," *IEEE Microwave and Guided Wave Letters,* Vol. 7, pp. 184-186, July, 1997.

12. R. F. Harrington, *Time-Harmonic Electromagnetic Fields*. New York: McGraw Hill, Inc., 1961.
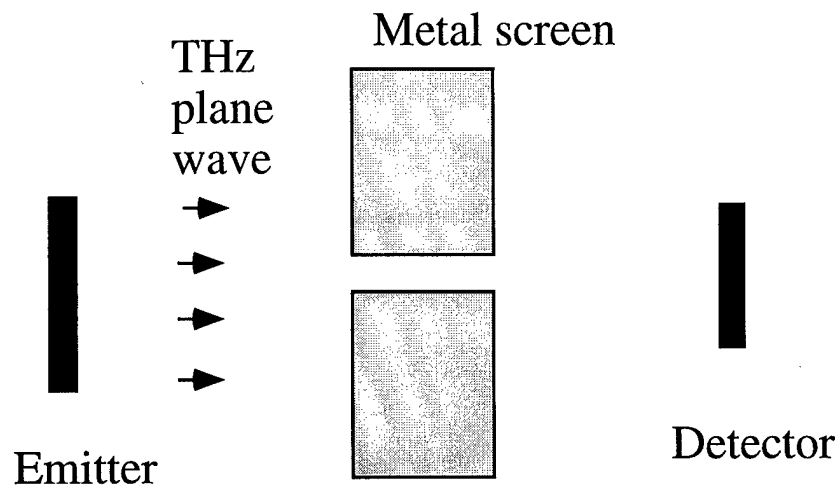
Figure Captions

Figure 1. Filtering of THz pulses: (a) Experimental setup, (b) Problem domain to be simulated. The parameters l and d are the length and thickness of the aperture, respectively.

Figure 2 The electric field in the aperture $E(x',y')$ can be used to calculate the far field $E_f(x,y)$. The aperture A is an opening in a metal plate that lies in the XY plane.

Figure 3 The distances from the four symmetric points in the plane containing the aperture to the far-field observation point are not the same, even though the E field values at the four points are equal.

Figure 4 Diagram of the reduced FDTD problem space. By using the near- to far-field transformation, any point in the far field can be calculated by the values in the aperture. Furthermore, by using symmetry, only one-fourth of the problem is simulated.

Figure 5 Comparison of the waveforms determined by the FDTD simulation directly (solid line) versus those determined by the transformation (dashed line). A plane wave Gaussian pulse of 0.375 picoseconds was passed through a rectangular aperture with a thickness of 1 mm and a width of 0.5 mm. The waveforms are at observation points perpendicular to the center axis (z direction) at distances of 0.24 mm (a) and 1.5 mm (b).

Figure 6 Comparison of the waveforms determined by the FDTD simulation directly (solid line) versus those determined by the transformation (dashed line). A plane wave Gaussian pulse of 0.375 picoseconds was passed through a rectangular aperture with a thickness of 1 mm and a width of 0.5 mm. The waveforms are at observation points 1.5 mm away in the z direction, but offset 4.5 mm in the y-direction (a) and x-direction (b).

Figure 7 Comparison of simulated versus the experimental data of Bromage, et al. [4]. (a) is the incident pulse and (b) is the resulting waveform after a rectangular aperture of 1.7 mm thickness and 0.5 mm width.

Figure 8. Resulting waveforms obtained by varying the thickness of a rectangular aperture with a width of 0.5 mm and a height of 0.15 mm.

Figure 9. Resulting waveforms obtained by varying the gap width of a rectangular aperture with a thickness of 0.225 mm and a height of 0.15 mm.
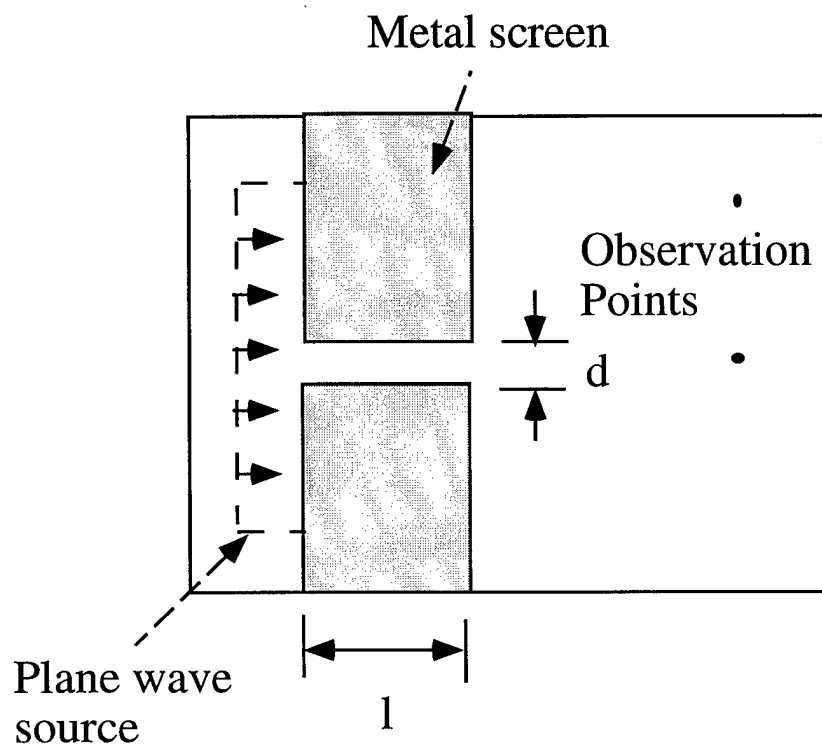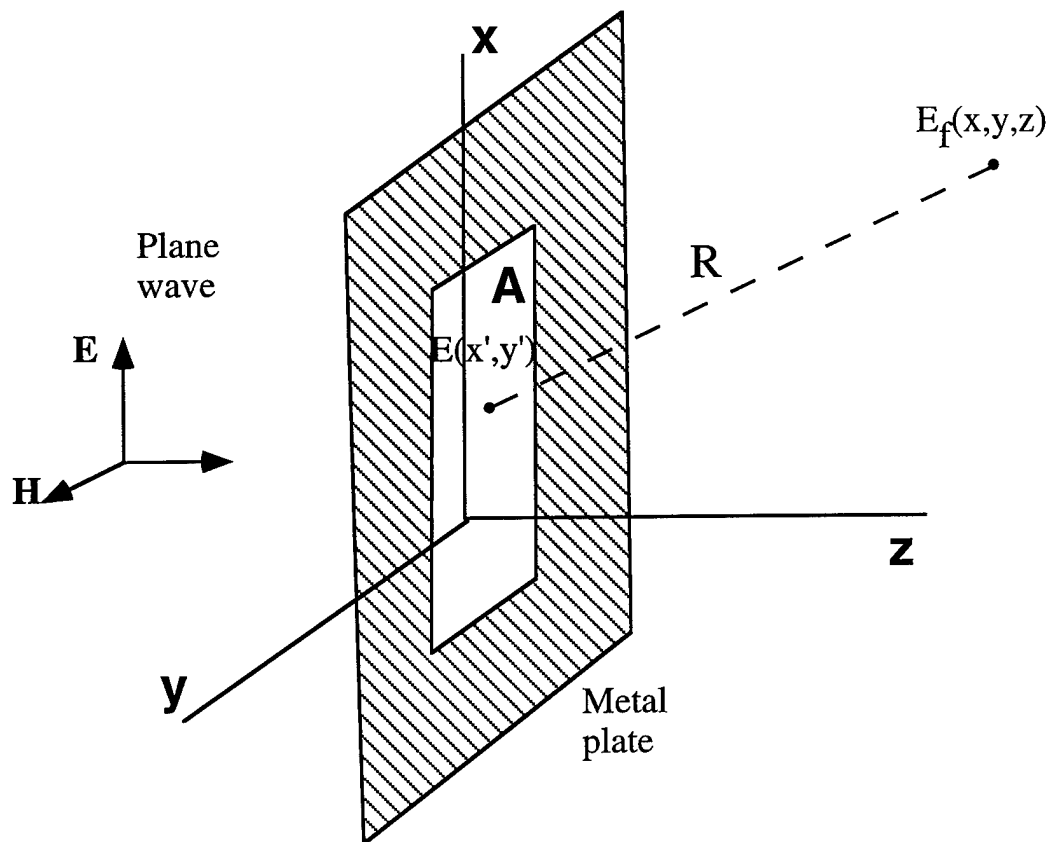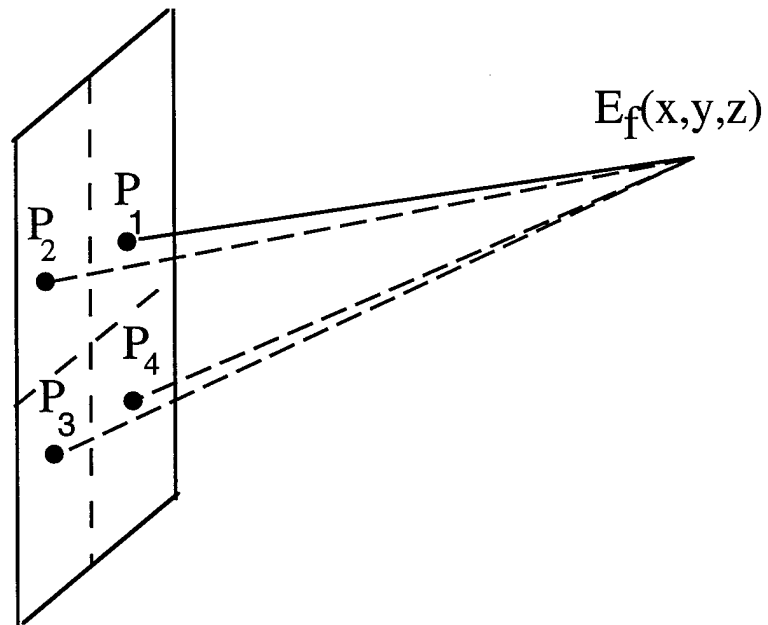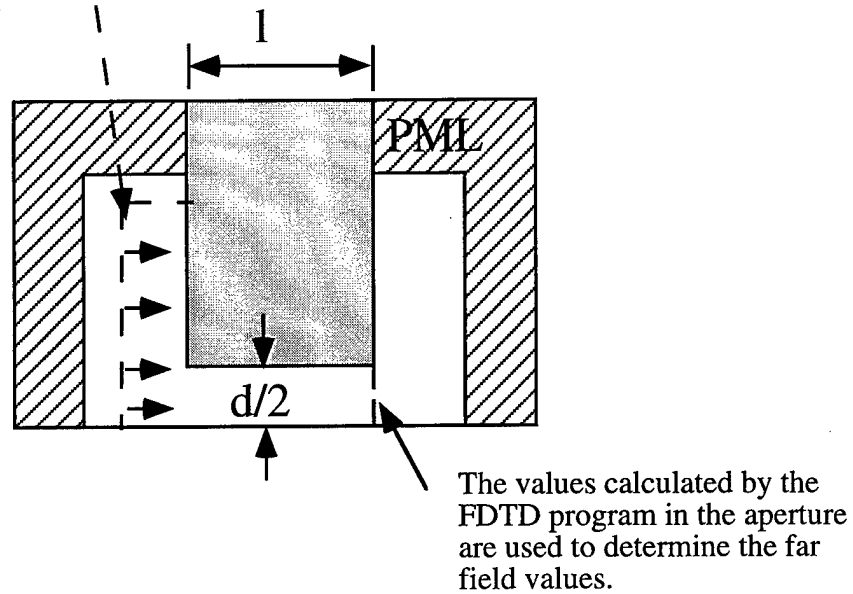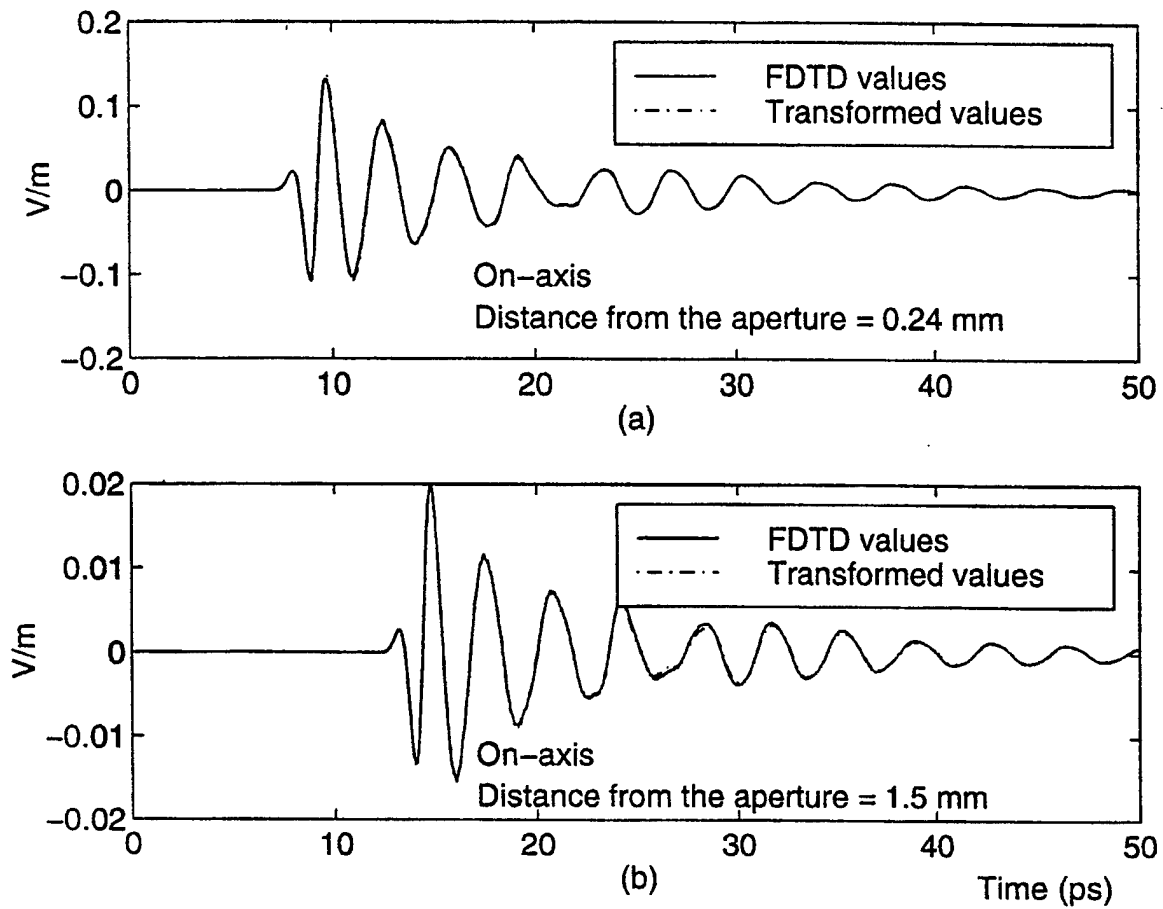
10

Figure 10. A tapered aperture.

Figure 11. Waveforms resulting from apertures tapered on one side (a) similar to Fig. 10, or tapered on both sides (b).

Figure 12. A circular aperture.

Figure 13 Waveforms resulting from circular apertures: (a) major radius 0.225 mm and a thickness of 0.15 mm, (b) major radius 0 .525 mm and thickness of 0.3 mm.

Figure 1. Filtering of THz pulses: (a) Experimental set up, (b) Problem domain to be simulated. The paramters l and d are the length and thickness of the aperture, respectively.

Figure 2. The electric field in the aperture E(x',y') can be used to calculate the far field $E_f(x,y,z)$. The aperture A is an opening in a metal plate that lies in the XY plane.

Figure 3. The distances from the four symmetric points in the plane containing the aperture to the far-field observation point are not the same, evan though the E field values at the four points are equal.

Figure 4. Diagram of the reduced FDTD problem space. By using
the near- to far-field transformation, any point in the far field can be
calculated by the values in the aperture. Furthermore, by using
symmetry, only one-forth of the problem is simulated.

Figure 5. Comparison of the waveforms determined by the FDTD simulation directly (solid lines) versus those determined by the transformation (dashed line). A plane wave Gaussian pulse of 0.375 picoseconds was passed through a rectangular aperture with a thickness of 1 mm and a width of 0.5 mm. The waveforms are at observation points perpendicular to the center axis (z direction) at distances of 0.24 mm (a) and 1.5 mm (b).

Figure 6. Comparison of the waveforms determined by the FDTD simulation directly (solid lines) versus those determined by the transformation (dashed line). A plane wave Gaussian pulse of 0.375 picoseconds was passed through a rectangular aperture with a thickness of 1 mm and a width of 0.5 mm. The waveforms are at observation points 1.5 mm away in the z direction, but offset .45 mm in the y direction (a) and x-direction (b).

Figure 7. Comparison of simulated versus experimental data of Bromage, et al. [4]. (a) is the incident pulse and (b) is the resulting wvaeform after a rectangular aperture of 1.7 mm thickness and 0.5 mm width.
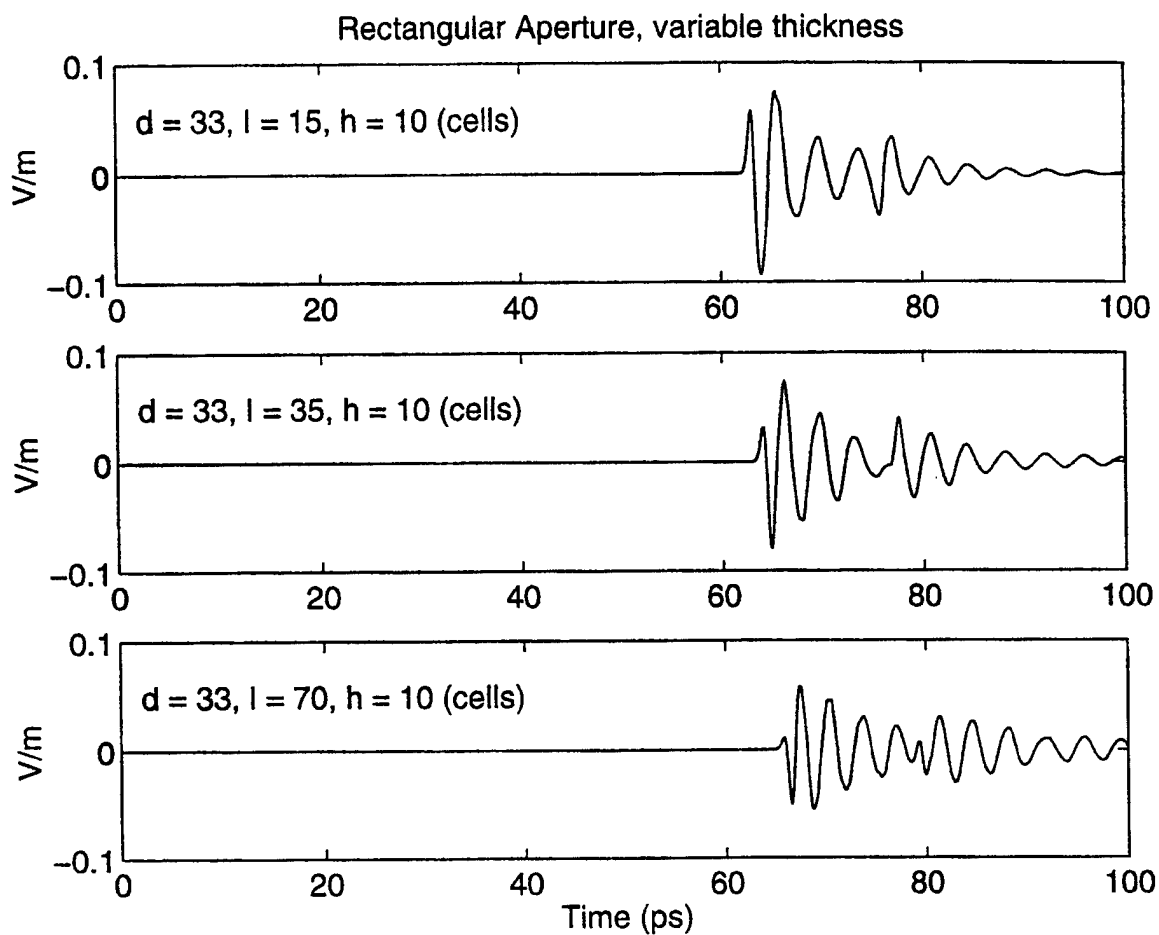
Figure 8. Resulting waveforms obtained by varying the thickness of a rectangular aperture witha width of 0.5 mm and a heightof 0.15 mm.
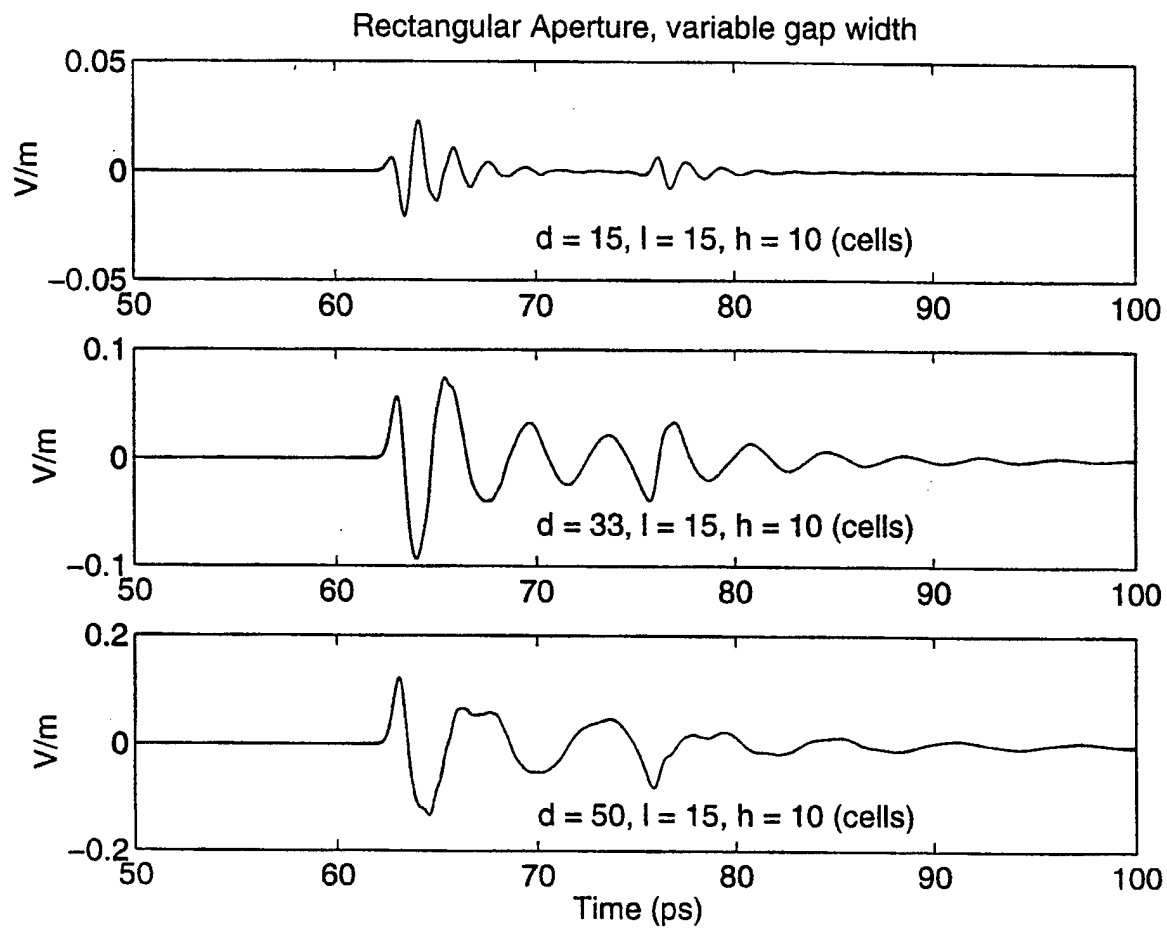
Figure 9. Resultingwaveforms obtained by varying the gap width of a rectangular aperture with a thickness of 0.225 mm and a height of 0.15 mm.
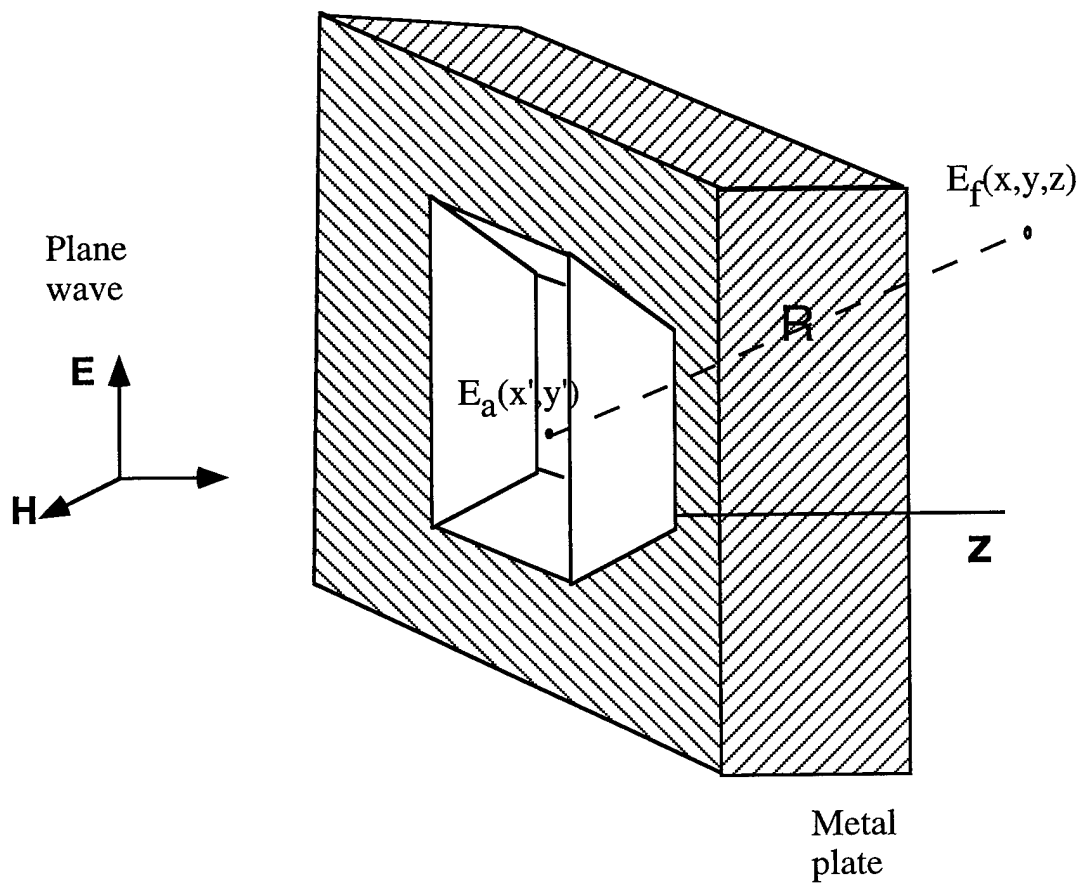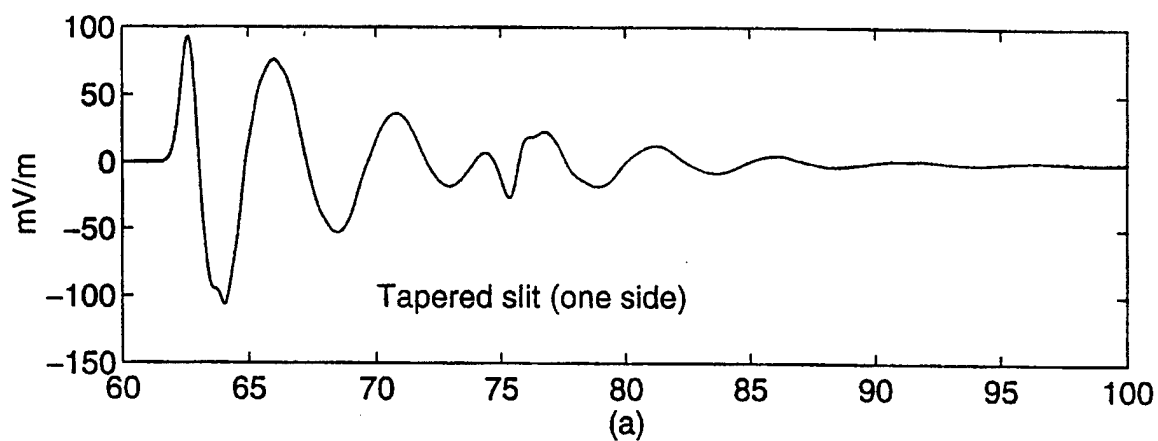
Figure 10. A tapered aperture.
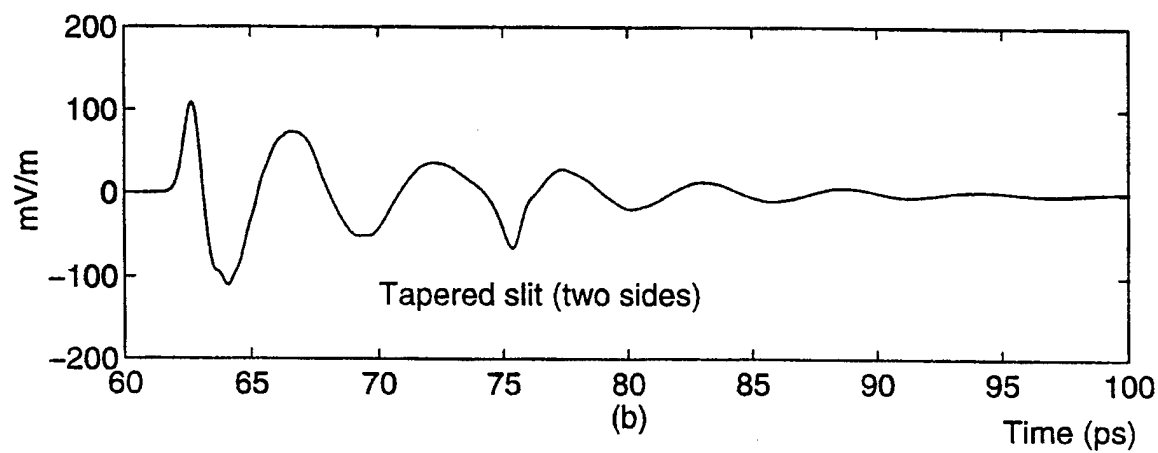
Figure 11. Waveforms resulting from aperuters tapered on one side (a) similar to Fig. 10, or tapered on both sides (b).
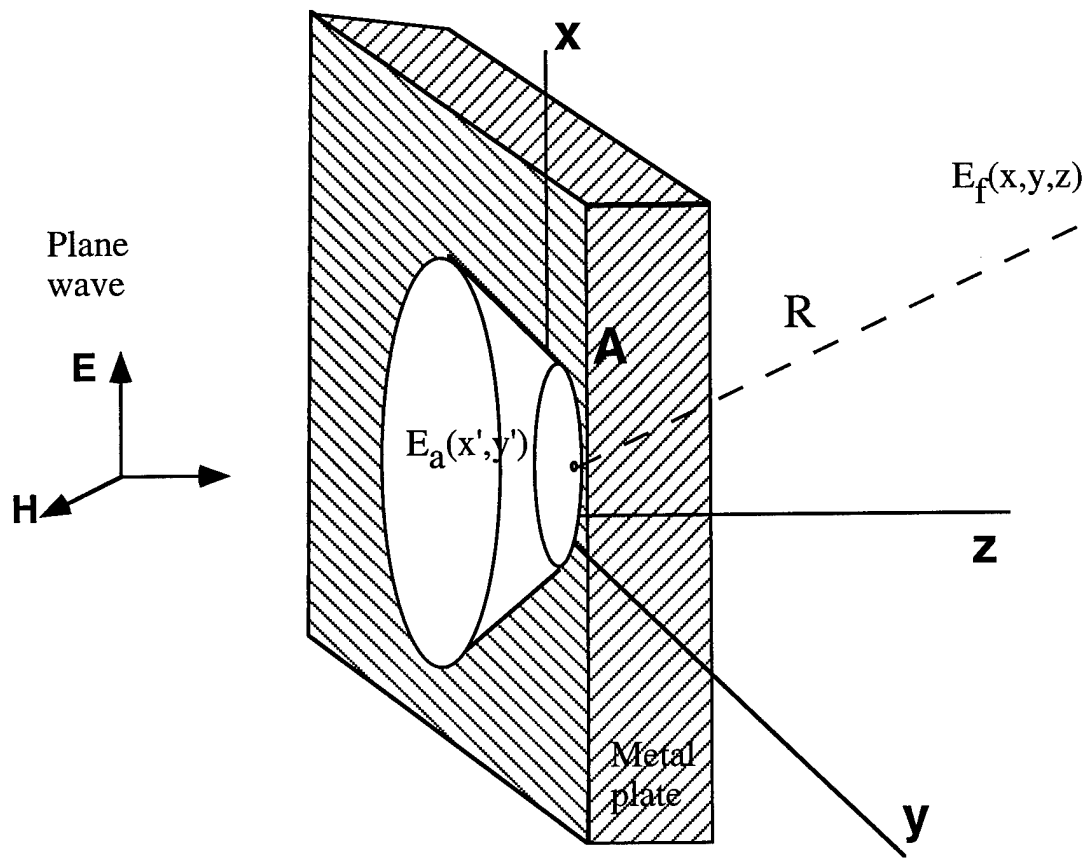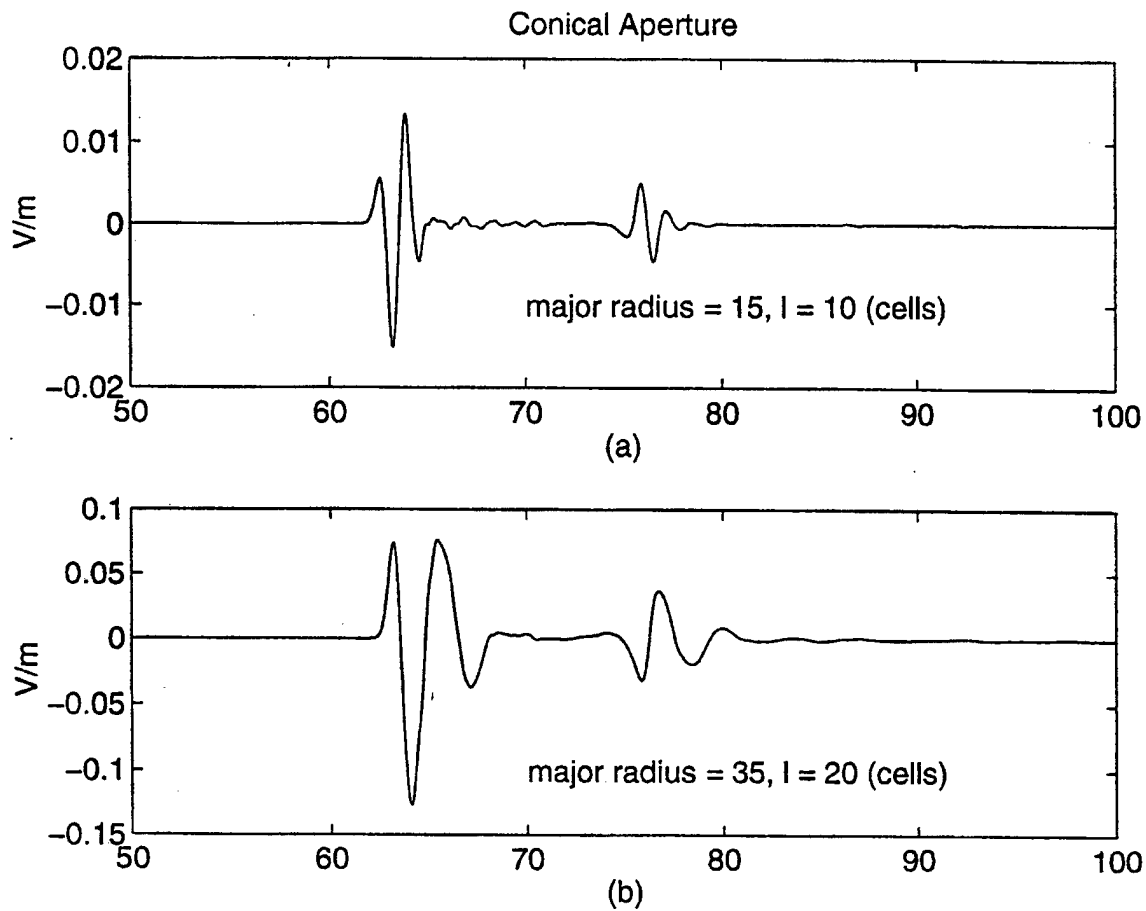
Figure 12. A circular aperture.

Figure 13. Waveforms resulting from circular apertuers: (a) major radius 2.25 mm and a thickness of 0.15 mm, (b) major radius 5.25 mm and thickness of 0.3 mm.